Computer Methods in Applied Mechanics and Engineering 461 (2026) 119224

Contents lists available at ScienceDirect

Computer Methods in Applied Mechanics and Engineering

journal homepage: www.elsevier.com/locate/cma

Topology optimization of additively manufactured continuous fiber-reinforced composites using B-spline components

Yifan Guo [a], Jikai Liu [c], Shuzhi Xu [b,*], Kentaro Yaji [b], Takayuki Yamada [a,*]

[a] Department of Mechanical Engineering, Graduate School of Engineering, The University of Tokyo, Yayoi 2–11–16, Bunkyo–ku, 113–8656, Tokyo, Japan
[b] Department of Mechanical Engineering, Graduate School of Engineering, The University of Osaka, 2-1, Yamadaoka, Suita, Osaka 565-0871, Japan
[c] School of Mechanical Engineering, Shandong University, Jinan, China

HIGHLIGHTS

- Explicit B-spline-driven framework for concurrent topology and fiber-path design.
- Spatially varying fiber density is enabled by local and global control.
- Path manufacturability ensured through proposed geometric constraints.
- Effective trade-off among stiffness, fiber density, and fiber usage.

GRAPHICAL ABSTRACT

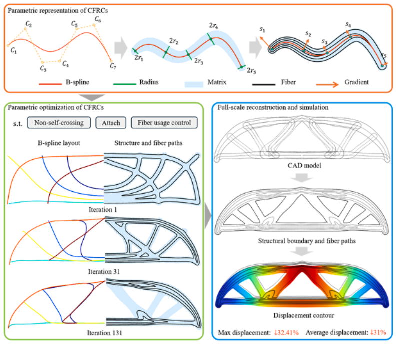

ARTICLE INFO

Keywords:
Topology optimization
Continuous fiber-reinforced composites
Additive manufacturing
B-spline components
Continuous fiber path generation
Fiber-content control

ABSTRACT

This paper proposes a B-spline-driven topology and fiber-path optimization framework for continuous fiber-reinforced composites (CFRCs). The structural layout is represented by multiple variable-width B-spline components, and continuous fiber paths are generated as iso-contours of a scalar field induced by these components. An additional spacing-control field is introduced to enable spatially varying path spacing and reinforcement allocation. To improve manufacturability, two process-oriented constraints are incorporated: a non-self-crossing constraint imposed on the control polygon of each component to prevent geometric artifacts caused by self-intersection, and an attachment constraint that progressively promotes smooth coupling between neighboring B-spline components, thereby producing more coherent fiber paths. In

* Corresponding authors.
E-mail addresses: xu@syd.mech.eng.osaka-u.ac.jp (S. Xu), t.yamada@mech.t.u-tokyo.ac.jp (T. Yamada).

https://doi.org/10.1016/j.cma.2026.119224
Received 10 April 2026; Received in revised form 13 June 2026; Accepted 5 July 2026
Available online 14 July 2026
0045-7825/

addition, local and global fiber-content constraints are introduced to control fiber spacing and overall fiber usage. The resulting iso-contour directions and analytically evaluated local fiber-density indicators are mapped to orthotropic effective material properties through a homogenization-based constitutive model. Adjoint sensitivities of the objective function and all constraints are derived with respect to the parametric design variables. Numerical examples show that the proposed method successfully generates optimized structures with continuous and manufacturable fiber paths, while full-scale simulations further verify their mechanical effectiveness: in the stiffness-oriented cases, the optimized-path design reduces the maximum and average displacements by up to 32.41% and 31.00%, respectively, compared with the reference fiber layouts; in the compliant-mechanism case, moderate fiber reinforcement increases the output displacement by 1.10% relative to the over-reinforced case, highlighting the trade-off between reinforcement and flexibility.

1. Introduction

Continuous fiber-reinforced composites (CFRCs) have attracted increasing interest in lightweight structural applications owing to their high specific stiffness and tailorable anisotropy [1,2]. Their mechanical performance depends critically on the continuity and spatial arrangement of deposited fiber trajectories, making fiber path design a primary driver of achievable reinforcement [3–6]. Recent advances in additive manufacturing further expand this design space by allowing fiber to be placed more freely along desired trajectories and enabling the concurrent design of structural topology and continuous fiber paths to more effectively utilize the reinforcement potential of CFRCs [7–10].

To fully exploit the potential of CFRCs, an effective design methodology must optimize structural topology and fiber paths within a unified framework. Topology optimization (TO) has matured over the past decades, yielding a broad class of approaches, including density-based methods [11], level-set methods [12,13], Bi-directional evolutionary structural optimization (BESO) method [14], and geometric parameterization schemes such as moving morphable components (MMC) method [15,16] and feature-driven method [17]. In parallel, additive manufacturing has stimulated the development of process-aware TO formulations that more closely connect structural design with fabrication constraints [18–23]. In the context of additively manufactured CFRCs (shown in Fig. 1), this trend naturally extends the design problem from pure structural layout optimization to the concurrent design of topology and reinforcement paths [24–29].

Current research on TO for CFRCs can be broadly classified into two categories according to how fibers are represented during optimization: discrete orientation representation and continuous path representation [30–32]. In the first category, the composite is usually modeled as an anisotropic material, and the local fiber direction is optimized on an element-wise basis. Representative approaches include the Solid Orthotropic Material with Penalization (SOMP) framework, in which fiber orientation is treated as a design variable coupled with the material distribution. For example, Yang et al. [33] developed a modified 3D SOMP TO method for CFRC shell structures under manufacturing constraints. Hou et al. [34] further proposed a curved-path-constrained SOMP (CPC-SOMP) formulation that incorporates fiber-path curvature effects into effective material properties. In parallel, Meng et al. [35] adopted SOMP in a concurrent optimization framework for simultaneously optimizing structural topology and fiber deposition paths under dynamic loads.

Another representative approach within discrete orientation representation is discrete material optimization (DMO), where multiple candidate fiber orientations are modeled as distinct material phases and interpolated to enable gradient-based optimization. In this line, Wu et al. [36] applied DMO to the orientation optimization of a composite laminate and demonstrated its effectiveness under multiple loading conditions. Ding and Xu [37] further extended this idea to a discrete–continuous setting by combining discrete material interpolation with continuous angle refinement. Similar discrete orientation treatments have also been used in ESO-based formulations [38,39]. More recently, machine-learning-based TO frameworks have also adopted related representations. For example, Liu et al. [40] developed a neural co-optimization framework in which structural topology, manufacturable layers, and path orientations are represented by implicit neural fields, while Chandrasekhar et al. [41] proposed FRC-TOuNN to simultaneously optimize matrix topology and fiber distribution using a mesh-independent representation.

Despite their effectiveness, discrete orientation representation faces persistent challenges in enforcing spatial continuity and

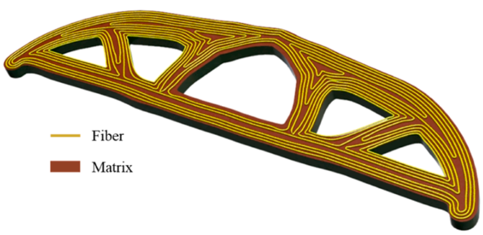

Fig. 1. Schematic illustration of an additively manufactured CFRCs MBB (Messerschmitt–Bölkow–Blohm) beam, showing the structural matrix domain and the embedded continuous fiber paths.

manufacturability of the orientation field. In practice, fiber deposition requires smooth, continuous trajectories, whereas element-wise orientation optimization often produces noisy fields and fragmented patterns that must be repaired through additional filtering [42–44], constraints [45–47], or post-processing [48]. Moreover, an optimized orientation field does not directly define a realizable toolpath, because a manufacturable continuous-fiber layout is inherently a global curve network subject to continuity, curvature, start/stop, and path-interaction constraints. Accordingly, several studies have attempted to bridge this gap by transforming discrete orientation information into continuous fiber trajectories [49–51]. For example, Wang et al. [52] proposed a stress-vector-tracing algorithm to generate continuous printing paths with variable spacing. Papapetrou et al. [53] developed an Equally-Space method (EQS) that concurrently considers structural topology and fiber paths to obtain variable-stiffness continuous-fiber designs. Liu et al. [54] further proposed a stress-driven infill mapping approach, where fiber paths are aligned with local stress vectors. However, such post-processing strategies for transforming discrete orientation fields into continuous paths still tend to introduce mismatches between the desired local fiber orientations and the resulting continuous fiber trajectories. Consequently, the TO process cannot directly employ material properties that are fully consistent with the final post-processed continuous fiber paths. Furthermore, because the path generation is performed sequentially after TO, manufacturing capabilities and constraints cannot be incorporated explicitly and directly into the optimization process.

The second category focuses on continuous path representation, which is more directly connected to fabrication because it produces printable trajectories during optimization. In this category, Li et al. [55] developed a collaborative TO framework in which structural topology and continuous fiber paths are co-designed through a level-set description of the geometry and a parameterized stream function for the fiber trajectories. In subsequent work, they proposed an efficient parallel framework [56] and further extended it to three-dimensional problems [57]. Xu et al. [58] proposed a TO method for additive manufacturing of CFRP structures based on an RBF-based level-set formulation, while Ho-Nguyen-Tan et al. [59] combined anisotropic TO and 3D printing to generate tailored continuous carbon-fiber paths directly from optimized structural boundaries.

In addition to these formulations, full-scale approaches have also been developed to represent continuous fiber paths explicitly [60]. For example, Li et al. [61] proposed a full-scale TO method for the concurrent design of structural topology, continuous fiber paths, and fiber morphology, including fiber volume, spacing, and thickness. Ren et al. [62] developed a full-scale concurrent optimization framework for structural topology and toolpath design in CFRC additive manufacturing, and later extended it to a manufacturability-aware co-design framework [63]. These studies have further advanced the integration of reinforcement-path design and fabrication-oriented optimization.

Among TO methodologies, explicit geometric parameterization schemes are particularly attractive because they describe structures by movable parameterized components that can be directly exported and reconstructed in Computer-Aided Design (CAD) environments [64,65]. Recent developments have enriched this class of methods by introducing flexible CAD primitives. For example, Zhu et al. [66] employed moving wide Bézier components with constrained ends to improve explicit geometric representation, Shannon et al. [67] introduced generalized Bézier components together with successive component refinement, Zhou et al. [68,69] developed multi-section B-spline offset features with enhanced deformability, and Zheng and Kim [70] combined MMC with non-uniform rational B-splines (NURBS)-curve boundaries to achieve smoother and more flexible boundary descriptions. These formulations offer explicit geometric controllability and natural compatibility with CAD-based reconstruction, and they have also been extended to composite design problems [71,72], where discrete orientation representation is still commonly adopted (e.g., assigning a constant fiber orientation to each component).

Overall, research on TO for CFRCs has gradually shifted fiber representation from discrete orientation fields toward continuous path representations that are more consistent with practical manufacturing. However, most continuous-path formulations are still based on level-set methods. In such methods, the ambiguity of fiber orientation may cause sign flips in the inferred orientation field, which can further lead to unintended breaks, junction artifacts, or discontinuities when the level-set-derived orientation information is converted into continuous paths. In addition, many level-set formulations generate fiber paths essentially by inward offsetting of the structural boundary, so that the resulting path distribution is governed mainly by geometric boundary features rather than by the intrinsic mechanical demand inside the structure. Such paths may also become problematic near the peak regions of the level-set function, where voids or overlaps can occur and degrade the fiber infill quality. By contrast, full-scale approaches can more faithfully capture manufacturable path details, but they usually involve much higher computational cost because detailed fiber-path geometry and related design interactions must be resolved explicitly during optimization.

To bridge the gap between topology representation and manufacturable fiber paths, this work proposes a B-spline-driven topology and fiber-path optimization framework for CFRCs fabricated by planar continuous-fiber extrusion. In this process, a continuous fiber tow, either pre-impregnated or co-extruded with a polymer matrix, is deposited through a moving nozzle along prescribed in-plane toolpaths. Accordingly, the key manufacturability requirements emphasized in this study include the generation of continuous fiber paths, avoidance of self-intersection and overlap between neighboring paths, suppression of excessive sharp turns, and controllable local fiber content or fiber spacing.

In the proposed framework, the structural geometry is represented by multiple variable-width B-spline components. Each component is defined by an explicit centerline, a radius field, and a spacing-control field, which together provide direct control over the component geometry, the associated length scale, and the local fiber spacing or reinforcement content. The fiber paths are not treated as fully independent design variables, but are generated as iso-contours of the scalar field induced by these components. Therefore, the structural layout, component geometry, fiber-path distribution, and local reinforcement allocation are consistently coupled through a compact set of parametric variables. As a result, the proposed framework integrates parametric topology representation, continuous fiber-path generation, manufacturability control, and reinforcement allocation for planar continuous-fiber deposition.

Compared with existing level-set-based continuous-path methods, the proposed framework provides a more explicit and compact geometric representation by assigning design variables to B-spline components rather than grid nodes or finite elements. This component-level description reduces the design-space dimension while enabling localized control of structural feature size, fiber-path spacing, and reinforcement distribution. Moreover, the explicit B-spline representation improves geometric interpretability and facilitates CAD-compatible reconstruction. In particular, the radius field associated with each B-spline centerline provides a direct mechanism for length-scale control during optimization.

The remainder of this paper is organized as follows. Section 2 introduces the proposed parametric framework, including geometry representation, fiber-path generation, homogenized modeling, and manufacturability constraints. Section 3 presents the optimization formulations and the overall computational procedure. Section 4 provides numerical examples to evaluate the proposed method in stiffness-oriented and compliant-mechanism design problems. Section 5 presents full-scale reconstruction and finite-element verification of representative optimized designs. Finally, Section 6 concludes the paper and outlines future research directions.

2. Methodology

This section outlines the proposed 2D framework for CFRCs. Variable-width B-spline components are first constructed to provide a parametric description of the structural geometry. Continuous fiber paths are then generated by iso-contour extraction from a distance-induced scalar field and mapped to effective material properties through a homogenization-based constitutive model. Finally, manufacturing constraints are introduced to ensure printable reinforcement layouts.

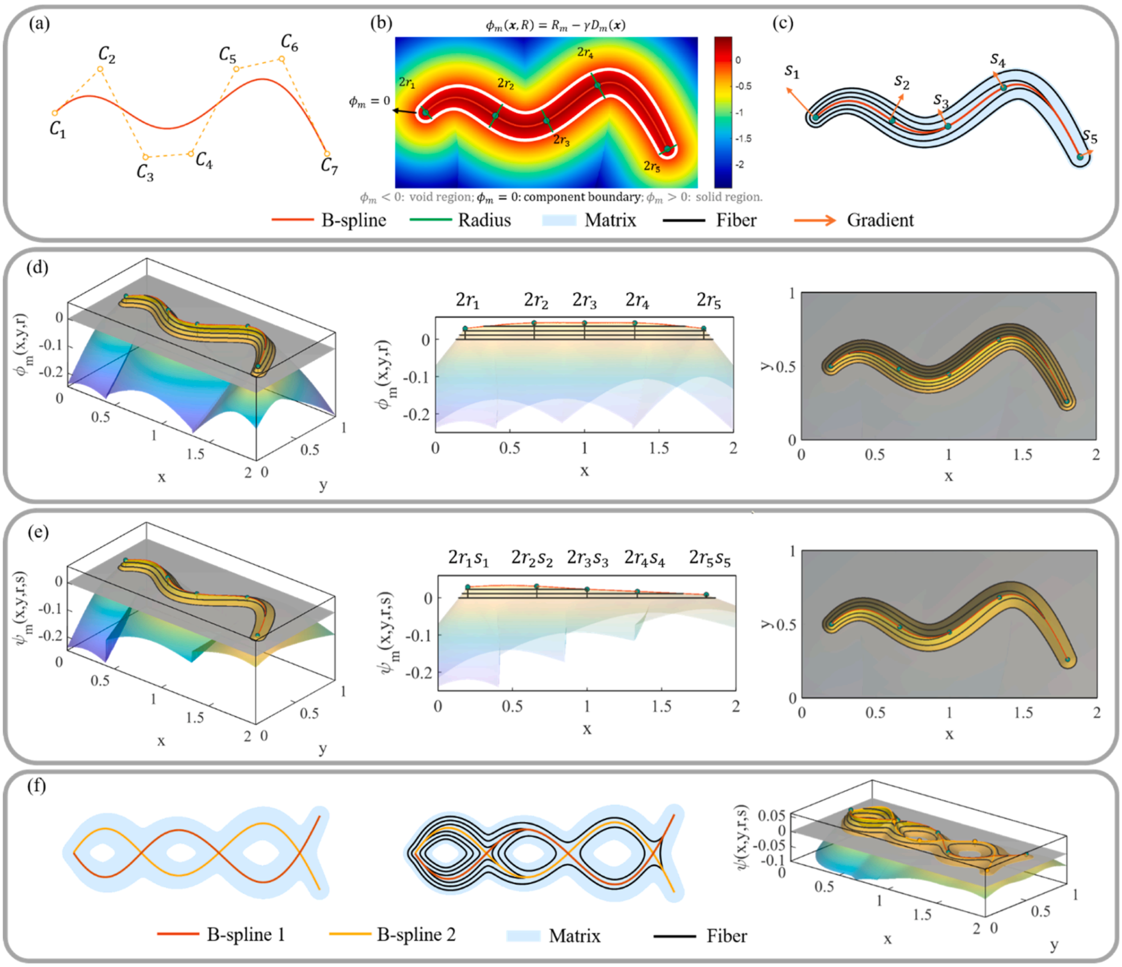

Fig. 2. Construction of a variable-width B-spline component and the associated continuous-fiber path field. (a) A B-spline centerline defined by the control points. (b) Graphical illustration of the variable-radius sweep level-set function in Eq. (6), where the highlighted zero contour defines the component boundary. (c) Continuous fiber trajectories represented by iso-contours inside the component. (d) The geometry-induced scalar field $\boldsymbol{\phi}_m$, and (e) spacing-controlled scalar field $\boldsymbol{\psi}_m$. (f) Multi-component coupling.

2.1. Parametric geometry and field construction

From each parametric B-spline component, two scalar fields are generated: a scalar field ϕ_m for implicit geometry representation and a companion field ψ_m for continuous fiber path extraction. Since the proposed method employs multiple B-spline components, the subscript m is used to denote the m-th B-spline component. The overall procedure is summarized in Fig. 2.

As shown in Fig. 2(a), the B-spline centerline is defined by:

$$\begin{aligned} &\mathscr{P}_m(\boldsymbol{\xi}) = \sum_{i=1}^{n_p} \mathscr{B}_i^{(p_p)}(\boldsymbol{\xi})\boldsymbol{C}_i, \\ &\{\boldsymbol{C}_i \in \mathbb{R}^2 \mid \boldsymbol{i} = 1,2,3,\ldots,\boldsymbol{n}_{sp}\}, \end{aligned} \tag{1}$$

where $\mathscr{B}_i^{(p_p)}(\xi)$ denotes the i-th B-spline basis function of degree p_p, defined over a non-decreasing knot vector, and ξ is the curve parameter and takes values in $[0\ 1]$. n_p is the number of control points. The control points $\boldsymbol{C}_i$ determine the geometric shape of the curve, while the basic functions provide local support and guarantee smoothness up to C^{p_p-1} continuity. This formulation enables compact and flexible parametric representation widely used in geometric modeling, CAD, and isogeometric analysis. In particular, B-splines form the polynomial basis of the more general NURBS, which are standard in CAD systems.

To construct a solid region from the 1D centerline, a spatially varying radius (half-width) field $R_m(\xi)$ is introduced, also parameterized by a 1D B-spline:

$$\begin{aligned} &\boldsymbol{R}_m(\boldsymbol{\xi}) = \sum_{j=1}^{n_r} \mathscr{B}_j^{(p_r)}(\boldsymbol{\xi})\boldsymbol{r}_j, \\ &\{\boldsymbol{r}_j \in \mathbb{R} \mid \boldsymbol{j} = 1,2,3,\ldots,\boldsymbol{n}_r\}, \end{aligned} \tag{2}$$

where r_j are the control variables correspond to the local cross-sectional radius, and n_r is the number of control points. The basic functions $\mathscr{B}_j^{(p_r)}(\xi)$ provide compact support and C^{p_r-1} continuity, ensuring a smooth transition of the radius along the entire channel. Moreover, since $\mathscr{B}_j(\xi) \geq 0$ and $\sum_j \mathscr{B}_j(\xi) = 1$, $R_m(\xi)$ is a convex combination of r_j, which implies

$$\boldsymbol{R}_m(\boldsymbol{\xi}) \in \left[\mathbf{min}(\boldsymbol{r}_j), \mathbf{max}(\boldsymbol{r}_j)\right]. \tag{3}$$

A minimum feature size can be enforced through simple bound constraints $r_j \geq r_{\min}$.

After obtaining the B-spline centerline, for any spatial point $\boldsymbol{x} \in \Omega \subset \mathbb{R}^2$, the closest parametric coordinate on the centerline is defined by

$$\boldsymbol{\Xi}_m(\boldsymbol{x}) = \underset{\xi\in[0,1]}{\mathbf{arg\ min}} \frac{1}{2} \| \boldsymbol{x} - \mathscr{P}_m(\boldsymbol{\xi}) \|^2, \tag{4}$$

and the corresponding Euclidean distance to the centerline is:

$$\boldsymbol{D}_m(\boldsymbol{x}) = \| \mathscr{P}_m(\boldsymbol{\Xi}_m(\boldsymbol{x})) - \boldsymbol{x} \| . \tag{5}$$

The m-th component geometry is implicitly represented by a variable-radius sweep level-set function:

$$\boldsymbol{\phi}_m(\boldsymbol{x}, \boldsymbol{R}) = \boldsymbol{R}_m - \boldsymbol{\gamma}\boldsymbol{D}_m(\boldsymbol{x}). \tag{6}$$

where γ is a numerical distance-scaling factor introduced to make γD comparable to R_m and improve the conditioning of the geometric representation. As illustrated in Fig. 2(b), the zero contour $\phi_m = 0$ defines the boundary of the swept B-spline component, with $\phi_m > 0$ representing the solid region and $\phi_m < 0$ representing the void region. The spatial distribution of ϕ_m is further shown in Fig. 2(d), which provides the basis for the subsequent fiber-path field construction.

Since the solid geometry is generated by sweeping a variable radius along the B-spline centerline, its iso-contours naturally form continuous fiber trajectories aligned with the local structural features. However, constant-level contour extraction produces nearly uniform path spacing and limits local reinforcement control. To enable spatially varying fiber spacing, an additional spacing-control field $S_m(\xi)$ is introduced along the centerline, as shown in Fig. 2(c):

$$\begin{aligned} &\boldsymbol{S}_m(\boldsymbol{\xi}) = \sum_{j=1}^{n_s} \mathscr{B}_j^{(p_s)}(\boldsymbol{\xi})\boldsymbol{s}_k, \\ &\{\boldsymbol{s}_k \in \mathbb{R} \mid \boldsymbol{k} = 1,2,3,\ldots,\boldsymbol{n}_s\}, \end{aligned} \tag{7}$$

where s_k are design variables controlling the local magnitude of the scalar-field gradient (and thus the path spacing). Extending S from the parametric coordinate to the spatial domain via the closest-point map gives:

$$\boldsymbol{S}_m(\boldsymbol{x}, \boldsymbol{s}) = \boldsymbol{S}_m(\boldsymbol{\Xi}_m(\boldsymbol{x}), \boldsymbol{s}). \tag{8}$$

The fiber path field is then defined as

$$\boldsymbol{\psi}_m(\boldsymbol{x},\boldsymbol{r},\boldsymbol{s}) = \boldsymbol{\phi}_m(\boldsymbol{x},\boldsymbol{r})\boldsymbol{S}_m(\boldsymbol{x},\boldsymbol{s}). \tag{9}$$

Importantly, multiplying by $S_m(\boldsymbol{x},s)$ does not change the zero-level set (i.e., $\psi_m(\boldsymbol{x}) = 0 \Leftrightarrow \phi_m(\boldsymbol{x}) = 0$), and therefore does not alter the structural boundary, and fiber trajectories extracted as iso-contours of ψ_m can be restricted to the interior of the solid region, ensuring that the generated paths are embedded within the manufactured structure. As illustrated in Fig. 2(e), the resulting field ψ_m locally adjusts the iso-contour spacing while maintaining continuous fiber trajectories within the solid region.

For a design consisting of M components, the assembled geometry and fiber path fields are constructed using a max-operator:

$$\phi(\boldsymbol{x},r,s) = \max(\phi_1,\phi_2,\ldots,\phi_m,\ldots,\phi_M),$$

$$\boldsymbol{\psi}(\boldsymbol{x},\boldsymbol{r},\boldsymbol{s}) = \max(\boldsymbol{\psi}_1,\boldsymbol{\psi}_2,\ldots,\boldsymbol{\psi}_m,\ldots,\boldsymbol{\psi}_M). \tag{10}$$

This choice is consistent with the sign convention in Eq. (6). Fig. 2(f) provides an illustrative example of the max-based coupling for two components. To ensure differentiability required by gradient-based optimization, the non-smooth max-operator in Eq. (10) is replaced by a Kreisselmeier–Steinhauser (KS) aggregation. Specifically, for a set of component fields, the assembled field is approximated as:

$$\boldsymbol{\phi}(\boldsymbol{x},\boldsymbol{r},\boldsymbol{s}) = \mathbf{KS}_{\max}(\boldsymbol{\phi}_1,\boldsymbol{\phi}_m,\ldots,\boldsymbol{\phi}_M) = \frac{1}{\beta}\ln\left(\sum_{m=1}^{M}\left(e^{\beta\boldsymbol{\phi}_m}\right)\right), \tag{11}$$

where $\beta > 0$ controls the tightness of the approximation to the maximum. As $\beta\to\infty$, $\phi(\boldsymbol{x},r,s)$ approaches the maximum, while for finite β it remains smooth and differentiable.

The computational domain is discretized using a background mesh of bilinear quadrilateral elements. The implicit description is converted to a 0−−1 material distribution via a Heaviside mapping. For an element with centroid $\boldsymbol{x}_e$, we define

$$\rho_e = \widetilde{H}(\boldsymbol{\phi}(\boldsymbol{x}_e)), \tag{12}$$

where $\rho_e \in [0,1]$ indicates the presence of material in element e ($\rho_e = 1$ for solid and $\rho_e = 0$ for void). $\widetilde{H}(\cdot)$ is a differentiable approximation of the Heaviside function,

$$\widetilde{H}(\boldsymbol{\phi}) = \begin{cases} 1 \textbf{ if } \boldsymbol{\phi} > \boldsymbol{\Delta}, \\ \dfrac{3(1-\alpha)}{4}\left(\dfrac{\boldsymbol{\phi}}{\boldsymbol{\Delta}} - \dfrac{\boldsymbol{\phi}^3}{3\boldsymbol{\Delta}^3}\right) + \dfrac{1+\alpha}{2} \textbf{ if } -\boldsymbol{\Delta} \le \boldsymbol{\phi} \le \boldsymbol{\Delta}, \\ \alpha \textbf{ otherwise}, \end{cases} \tag{13}$$

where Δ is the parameter to control the magnitude of the smoothing interval. α is taken as a very small positive number to avoid the singularity of the stiffness matrix.

2.2. Homogenized fiber model construction

After obtaining the continuous fiber path field, an orthotropic constitutive model is constructed through a homogenization procedure. As shown in Fig. 3, the local fiber direction is derived from the iso-contour tangent direction, while the local fiber-density indicator is analytically evaluated from the component-wise spacing-control fields and KS ownership weights.

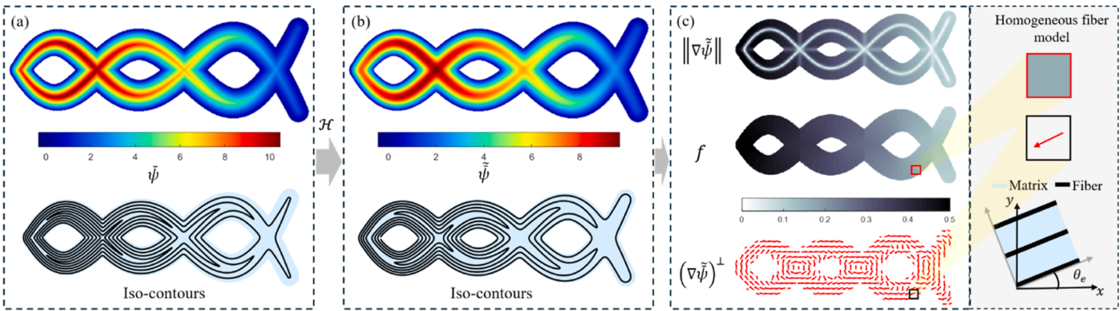

Fig. 3. Continuous fiber-path generation and construction of the homogenized fiber model. (a) Normalized assembled scalar field $\widetilde{\psi}$ and the extracted iso-contours. (b) Filtered scalar field $\widetilde{\widetilde{\psi}}$ and the corresponding smoothed iso-contours after applying the scalar-field smoothing operation. (c) Evaluation of local field quantities, including the scalar-field gradient, analytical fiber-density indicator, and fiber direction, followed by the construction of the homogenized fiber-reinforced material model from the local fiber density and orientation. (Note: $(\nabla\widetilde{\widetilde{\psi}})^{\perp}$ denotes the vector orthogonal to $\nabla\widetilde{\widetilde{\psi}}$, i.e., a 90° rotation in 2D.)

2.2.1. Fiber-path field evaluation

To obtain a dimensionless scalar field and make the field variation comparable across different mesh resolutions, the assembled fiber-path scalar field ψ is normalized as:

$$\bar{\psi}(\boldsymbol{x}) = \frac{\psi(\boldsymbol{x})}{\gamma h}, \tag{14}$$

where h is the background element size and γ is the distance-scaling factor introduced in Eq. (6).

As shown in Fig. 3(a), the iso-contours directly extracted from $\bar{\psi}$ may exhibit local sharp turns. This is mainly caused by the ridge-type structure of the distance-induced scalar field near the B-spline skeleton. In this region, the one-sided gradient directions on the two sides of the skeleton may be opposite, and the curvature evaluation of the implicit contour field can become numerically ill-conditioned. To alleviate this local non-smoothness and obtain smoother fiber paths, a normalized convolution smoothing operation is applied to the normalized assembled scalar field:

$$\tilde{\bar{\psi}} = \mathscr{H}(\bar{\psi}), \tag{15}$$

where $\mathscr{H}$ denotes a normalized convolution-type smoothing operator. As demonstrated in Fig. 3(b), this scalar-field smoothing reduces sharp turns caused by the ridge-type distance-field representation while preserving the overall topology and the contour-based fiber-path generation mechanism.

The spatial gradients of the smoothed scalar field at the centroid of element e are evaluated as

$$\varphi_x = \frac{\partial \tilde{\bar{\psi}}}{\partial x}, \ \varphi_y = \frac{\partial \tilde{\bar{\psi}}}{\partial y}. \tag{16}$$

The continuous fiber paths are then extracted as iso-contours of $\tilde{\bar{\psi}}$. Since $\nabla\tilde{\bar{\psi}}$ is normal to an iso-contour, the local fiber direction is naturally defined as the tangent direction of the iso-contour. Therefore, the corresponding fiber angle is computed as:

$$\theta_e = \mathbf{atan2}\left(-\varphi_x, \varphi_y\right), \tag{17}$$

It should be noted that the local fiber-density indicator is not evaluated from the numerical gradient magnitude of the assembled scalar field. Otherwise, opposite one-sided gradients near the B-spline skeleton may cancel under central-difference-type numerical evaluation, leading to a nonphysical near-zero fiber-density band, as illustrated in Fig. 3(c). To avoid this artifact, the fiber-density indicator is evaluated analytically from the component-wise spacing-control fields used in Eq. (9).

For a point $\boldsymbol{x}$ influenced by multiple B-spline components, the contribution of each component is determined by the same KS aggregation used for the assembled fiber-path field. Specifically, the soft ownership weight of the m-th component is defined as

$$w_m = \frac{e^{\beta\psi_m(\boldsymbol{x},\boldsymbol{r},\boldsymbol{s})}}{\sum_{i=1}^{M} e^{\beta\psi_i(\boldsymbol{x},\boldsymbol{r},\boldsymbol{s})}}, \tag{18}$$

where β is the KS aggregation parameter. The local fiber-density indicator is then defined as the weighted contribution of all component-wise spacing-control fields:

$$f = \sum_{m=1}^{M} w_m S_m(\boldsymbol{x}, \boldsymbol{s}). \tag{19}$$

With this definition, the fiber-density indicator at each point is mainly governed by the dominant component while remaining smooth and differentiable in regions where multiple components overlap. It should also be noted that small gaps may still appear after de-homogenization, since a finite solid region may not always accommodate an integer number of discrete filament paths with the prescribed spacing [58].

2.2.2. Orthotropic constitutive interpolation

Given θ_e and f_e, each element is modeled as an orthotropic lamina whose principal material axis aligns with the fiber direction. The effective engineering constants in the local material coordinates are obtained by a mixture rule [73]:

$$\begin{cases} E_{1,e} = E_1^{\mathrm{f}} f_e + E_1^{\mathrm{m}}(1-f_e), \\ E_{2,e} = E_2^{\mathrm{f}} E_2^{\mathrm{m}} \Big/ \left(E_2^{\mathrm{m}} f_e + E_2^{\mathrm{f}}(1-f_e)\right), \\ G_{12,e} = G_{12}^{\mathrm{f}} G_{12}^{\mathrm{m}} \Big/ \left(G_{12}^{\mathrm{m}} f_e + G_{12}^{\mathrm{f}}(1-f_e)\right), \\ \nu_{12,e} = \nu_{12}^{\mathrm{f}} f_e + \nu_{12}^{\mathrm{m}}(1-f_e), \\ \nu_{21,e} = \left(E_{2,e}/E_{1,e}\right)\nu_{12,e}. \end{cases} \tag{20}$$

Under plane stress, the local compliance matrix is:

$$\mathbf{D}_e^0 = \begin{bmatrix} \dfrac{E_{1,e}}{1-\nu_{12,e}\nu_{21,e}} & \dfrac{\nu_{12,e}E_{2,e}}{1-\nu_{12,e}\nu_{21,e}} & 0 \\ \dfrac{\nu_{21,e}E_{1,e}}{1-\nu_{12,e}\nu_{21,e}} & \dfrac{E_{2,e}}{1-\nu_{12,e}\nu_{21,e}} & 0 \\ 0 & 0 & G_{12,e} \end{bmatrix}. \tag{21}$$

The constitutive matrix in the global coordinates can be calculated via:

$$\mathbf{D}_{e,\theta}^0(\theta_e) = \mathbf{T}(\theta_e)^T \mathbf{D}_e^0 \mathbf{T}(\theta_e), \tag{22}$$

where $\mathbf{T}(\theta)$ is the rotation matrix. Finally, the effective constitutive matrix is interpolated as:

$$\mathbf{D}_e = \rho_e^p \mathbf{D}_{e,\theta}^0(\theta_e), \tag{23}$$

and the element stiffness is assembled as:

$$\mathbf{k}_e = \int_{\Omega_e} \mathbf{B}^T \mathbf{D}_e \mathbf{B} \mathrm{d}\Omega, \tag{24}$$

with $\mathbf{B}$ denoting the strain–displacement matrix. Assembling the elemental stiffness matrices $\mathbf{k}_e$ over all elements produces the global stiffness matrix $\mathbf{K}$, thereby completing the finite-element discretization of the orthotropic CFRCs constitutive response induced by the optimized fiber path field.

2.3. Manufacturability constraints

During optimization, the movement of B-spline control points may introduce artifacts into the induced fiber-path field. Fig. 4 illustrates the manufacturability-related constraints considered in this work. As shown in Fig. 4(a), self-intersection of a B-spline component may produce an invalid component skeleton and introduce geometric artifacts into the induced scalar field. To avoid this issue, the non-self-crossing constraint is imposed on the control polygon. The sampling points and admissible point pairs used to evaluate this constraint are illustrated in Fig. 4(b).

In addition, when neighboring B-spline components become nearly touching without proper attachment, irregular local contours or spurious loops may appear in the extracted fiber paths, as shown in Fig. 4(c). Therefore, an attachment constraint is introduced to

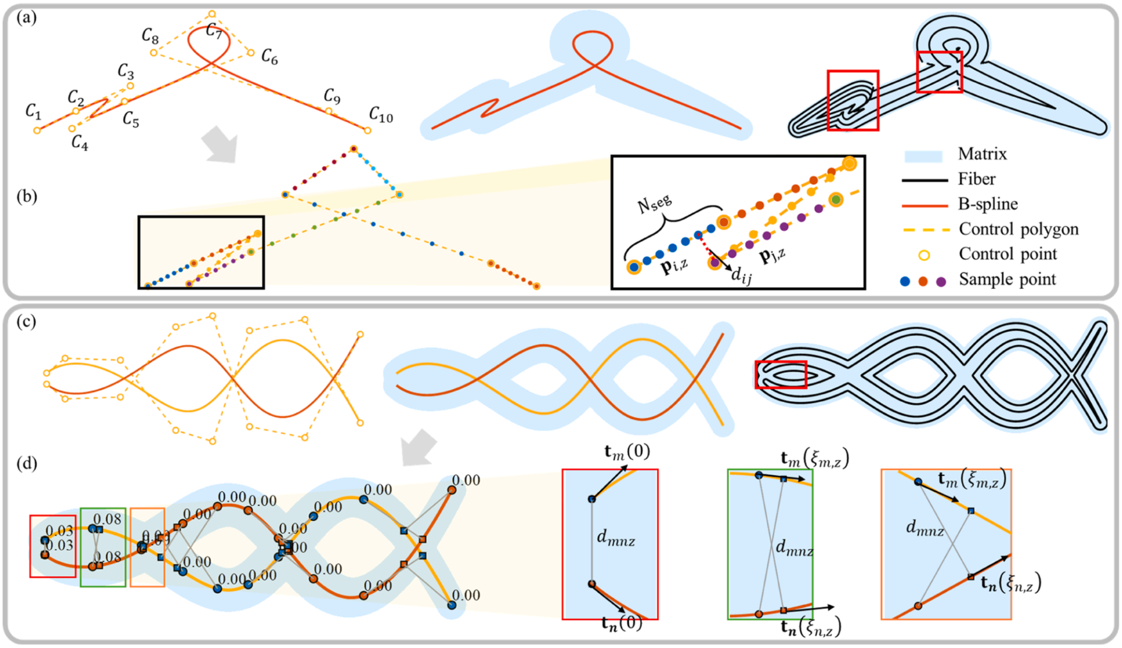

Fig. 4. Schematic illustration of the proposed manufacturability constraints. (a) Self-intersection of a B-spline component and the resulting geometric artifact. (b) Sampling on the control polygon and enlarged view of admissible point pairs used to define the non-self-crossing constraint. (c) Artifacts arising when neighboring B-spline components become nearly touching without proper attachment. (d) Sampling on the B-spline centerlines and enlarged view of admissible point pairs used to define the attachment constraint.

promote smooth connection between neighboring components. Fig. 4(d) illustrates the sampling strategy on the B-spline centerlines and the admissible point pairs used to define the attachment constraint.

2.3.1. Non-self-crossing constraint formulation

To prevent self-intersection, a non-self-crossing constraint is imposed on the control polygon of each B-spline component. For a component with control points $\mathbf{C}_i$, the control polygon consists of the following line segments:

$$\mathscr{S}_i = \mathbf{C}_i\mathbf{C}_{i+1}, i = 1, \dots, n_p - 1. \tag{25}$$

On each segment $\mathscr{S}_i$, we sample N_{seg} points using a uniform set of parameters $t_z \in [0,1]$ (see Fig. 4(b)):

$$\mathbf{p}_{i,z} = (1 - t_z)\,\mathbf{C}_i + t_z\,\mathbf{C}_{i+1}. \tag{26}$$

To avoid penalizing the inherent proximity of neighboring polyline segments, we only consider point pairs whose underlying segments are non-adjacent:

$$\mathscr{A}_m = \{(i,j)|1 \le i\langle j \le n_p - 1, |i-j|\rangle 1\}. \tag{27}$$

For each admissible pair $(i,j) \in \mathscr{A}_m$, define the distance (see Fig. 4(b)) and violation

$$d_{ij} = \| \mathbf{p}_i - \mathbf{p}_j \|, \ \nu_{ij} = d_{\min} - d_{ij}, \tag{28}$$

where $d_{\min}$ is the prescribed minimum separation. Enforcing $v_{ij} \le 0$ for all admissible pairs prevents self-intersection and maintains a minimum geometric clearance of the control polygon. To obtain a single constraint per component, v_{ij} is aggregated using the KS function:

$$g_m^{\text{self}} = \mathbf{KS}_{\max}(\nu_{ij}) - \varepsilon \le 0, m = 1, \dots, M, \tag{29}$$

where ε is a small inactive margin, set to 10^{-6} in this paper.

2.3.2. Attachment constraint

To alleviate artifacts arising when neighboring components become nearly tangent, nearly touching, or weakly overlapping, an attachment constraint is introduced to promote geometrically consistent attachment between neighboring components. For each component m, N_{att} parametric locations $\xi_z \in [0,1]$are sampled along its centerline B-spline $\mathscr{P}_m$. The corresponding physical point is

$$\mathbf{p}_{m,z} = \mathscr{P}_m(\xi_{m,z}), z = 1, \dots, N_{\text{att}}. \tag{30}$$

Unlike the non-self-crossing constraint, which samples the control polygon to obtain a direct and explicit dependence on the control point design variables, the attachment constraint samples points on the B-spline centerline, enabling more accurate control of the B-spline geometry. For each $\mathbf{p}_{m,z}$, its distance to any other component $n \ne m$ is evaluated through the closest-point projection defined in Eq. (4):

$$\xi_{n,z} = \Xi_n(\mathbf{p}_{m,z}), \tag{31}$$

and the corresponding Euclidean distance is (see Fig. 4(d)):

$$d_{m,n,z} = \| \mathscr{P}_n(\xi_{n,z}) - \mathbf{p}_{m,z} \|. \tag{32}$$

Let $R_m(\xi_{m,z})$ and $R_n(\xi_{n,z})$ be the local half-widths of components m and n at the corresponding parametric coordinates. An overlap indicator is defined

$$\varrho_{m,n,z} = R_m(\xi_{m,z}) + R_j(\xi_{n,z}) - d_{m,n,z}, \tag{33}$$

where $\varrho_{m,n,z}$ is an overlap indicator for the solids generated by components m and n at sample z. When overlap is detected, coincidence of the two center B-spline curves is desired at this sample, particularly when the two centerlines are nearly parallel.

To allow sharp crossings and junctions in the interior, a tangent-compatibility condition for non-endpoint samples is also imposed. The unit tangents are

$$\mathbf{t}_m(\xi_{m,z}) = \frac{\mathscr{P}'_m(\xi_{m,z})}{\| \mathscr{P}'_m(\xi_{m,z}) \|}, \ \mathbf{t}_n(\xi_{n,z}) = \frac{\mathscr{P}'_n(\xi_{n,z})}{\| \mathscr{P}'_n(\xi_{n,z}) \|}. \tag{34}$$

Then,

$$\sigma_{m,n,z} = |\mathbf{t}_m^{\mathrm{T}}\mathbf{t}_n| - \cos(\omega), \tag{35}$$

where ω is a prescribed angular threshold. Hence, σm,n,z>0 indicates that the two tangents are aligned within ω (allowing both co-directional and anti-directional alignment). For endpoint samples (ξ=0 or 1), the tangent constraint can be omitted to allow endpoint attachment more flexibly. To combine proximity and angle requirements in a differentiable manner, a smooth approximation of the minimum is used again:

$$\boldsymbol{\mu}_{m,n,z} = -\mathbf{KS}_{\max}\left(-\varrho_{m,n,z}, -\boldsymbol{\sigma}_{m,n,z}\right), \tag{36}$$

while for endpoint samples we simply take $\mu_{m,n,z} = \varrho_{m,n,z}$.

The attachment constraint is intended to be active only when two components are likely to overlap and their centerlines are nearly parallel, i.e., when the interaction indicator $\mu_{m,n,z}$ becomes positive. To preserve differentiability, a smooth gate function $G_{m,n,z}\in[0,1]$ is introduced using the Heaviside approximation in Eq. (13),

$$\boldsymbol{G}_{m,n,z} = \widetilde{\boldsymbol{H}}\left(\boldsymbol{\mu}_{m,n,z}\right), \tag{37}$$

where $G_{m,n,z} = 0$ implies that the pair (m, n) is inactive, while $G_{m,n,z}=1$ indicates an active candidate for attachment.

For an active pair, we enforce a target attachment distance d_{att} through

$$\boldsymbol{\eta}_{m,n,z} = \boldsymbol{G}_{m,n,z}\left(\boldsymbol{d}_{m,n,z} - \boldsymbol{d}_{\text{att}}\right), \tag{38}$$

so that $\eta_{m,n,z} \le 0$ encourages the interacting components to "snap" into a consistent attachment configuration (distance not exceeding d_{att}), which empirically suppresses ridges and improves the smoothness of the assembled fiber field. Since multiple neighboring components may exist, we aggregate $\{\eta_{m,n,z}\}_{n\neq m}$ into a single per-sample scalar:

$$\boldsymbol{g}_{m,z} = \mathbf{KS}_{\max}\left(\{\boldsymbol{\eta}_{m,n,z}\}_{n\neq m}\right), \tag{39}$$

Finally, one constraint per component m by averaging over all samples is formulated:

$$\boldsymbol{g}_m^{\text{conn}} = \frac{1}{\boldsymbol{N}_{\text{att}}}\sum_{z=1}^{\boldsymbol{N}_{\text{att}}}\boldsymbol{g}_{m,z} - \varepsilon \le 0, \boldsymbol{m} = 1, \ldots, \boldsymbol{M}. \tag{40}$$

2.3.3. Fiber-content constraints

To control printability and material usage, two fiber content constraints are imposed. To ensure that these constraints act only on the solid phase, we mask the fiber content by the physical density ρ_e and define the effective (solid phase) fiber content as:

$$\widetilde{f}_e = \rho_e f_e. \tag{41}$$

2.3.3.1. Local maximum fiber density constraint. To prevent excessive local reinforcement (which may violate manufacturability or lead to overly dense paths), the maximum effective fiber content is constrained. A differentiable global maximum approximation of $\widetilde{f}_e$ is constructed via a p-norm:

$$\widetilde{f}_{\max} = \left(\sum_{e=1}^{N_e}\widetilde{f}_e^{\,p_n}\right)^{1/p_n}, \tag{42}$$

where $p_n > 1$ is the aggregation exponent that controls the tightness of the max-approximation, and the constraint is written as

$$g_{\text{loc}} = \frac{\widetilde{f}_{\max}}{f_0} - 1 \le 0, \tag{43}$$

where f_0 is the prescribed upper bound on the effective fiber content.

2.3.3.2. Global fiber-usage constraint. Due to the high cost of continuous fibers, it is desirable to limit the overall fiber usage. Accordingly, a global usage constraint is imposed:

$$\bar{f} = \frac{1}{NV_0}\sum_{e=1}^{N}\widetilde{f}_e, \tag{44}$$

where N denotes the number of background elements, V_0 is the prescribed maximum volume fraction, and the corresponding constraint is defined as

$$g_{\text{glob}} = \frac{\bar{f}}{V_f} - 1 \le 0, \tag{45}$$

where V_f is the allowable global fiber volume.

3. Optimization model formulation

To demonstrate the effectiveness of the proposed optimization framework, both stiffness-oriented and compliant-mechanism design problems are considered in this work. The design variables consist of the B-spline control points, the radius controls, and the spacing controls:

$$\boldsymbol{\lambda} = \left(\mathbf{C}_{m,i},\ r_{m,j},\ s_{m,k}\right)_{m=1}^{M}. \tag{46}$$

For a given $\boldsymbol{\lambda}$, the assembled geometry field $\phi(\boldsymbol{x})$ and fiber path field $\psi(\boldsymbol{x})$ are constructed as described in Sections 2.1. The physical density (ρ_e) is obtained by the smoothed Heaviside projection, and the fiber orientation θ_e and fiber content indicator f_e are computed (Section 2.2.1), which together define the orthotropic constitutive matrix $\mathbf{D}_e$ (θ_e, f_e). The equilibrium equation is then solved to obtain the displacement field $\mathbf{U}$. The resulting optimization problem is formulated as:

$$\begin{cases} \text{find} : \boldsymbol{\lambda} \\ \min : c(\boldsymbol{\lambda}) \\ \text{s.t.}\ \mathbf{K}(\mathbf{U})\mathbf{U} = \mathbf{F}, \\ V(\rho) \leq V_0, \\ g_{\text{loc}}(\boldsymbol{\lambda}) = \dfrac{\widetilde{f}_{\max}}{f_0} - 1 \leq 0, \\ g_{\text{glob}}(\boldsymbol{\lambda}) = \dfrac{\bar{f}}{V_{\text{f}}} - 1 \leq 0, \\ g_m^{\text{self}}\left(\mathbf{C}_{m,i}\right) \leq 0, \\ g_m^{\text{conn}}\left(\mathbf{C}_{m,i}\right) \leq 0, \\ \mathbf{C}_{m,i} \in \Omega_{\text{adm}}, \\ r_{m,j} \in \left[r_{\min}, r_{\max}\right], \\ s_{m,k} \in \left[s_{\min}, s_{\max}\right]. \end{cases} \tag{47}$$

Here, $c(\boldsymbol{\lambda})$ denotes the objective function, $V(\rho)$ represents the material volume fraction in the design domain, and V_0 is the prescribed upper limit of this volume fraction. The remaining constraints of the optimization model have been introduced in the preceding sections.

Fig. 5 summarizes the overall workflow of the proposed framework.

Step 1: Initialization. The background mesh, projection parameters, and design variables, including the B-spline control points $\mathbf{C}_{m,i}$, radius controls $r_{m,j}$, and spacing controls $s_{m,k}$, are initialized.

Step 2: Geometry and fiber-field construction. The scalar fields are constructed and assembled to form the structural field $\phi(\boldsymbol{x})$ and the fiber-path field $\psi(\boldsymbol{x})$, while the non-self-crossing and attachment constraints are evaluated. The assembled geometry field is then projected to density variables ρ.

Step 3: Fiber model and response analysis. The gradient of the smoothed fiber-path scalar field is used to extract the fiber orientation, while the fiber-density indicator is analytically evaluated from the spacing-control fields and KS ownership weights. The orthotropic fiber model is then constructed, and finite element analysis is performed to obtain the structural response under the

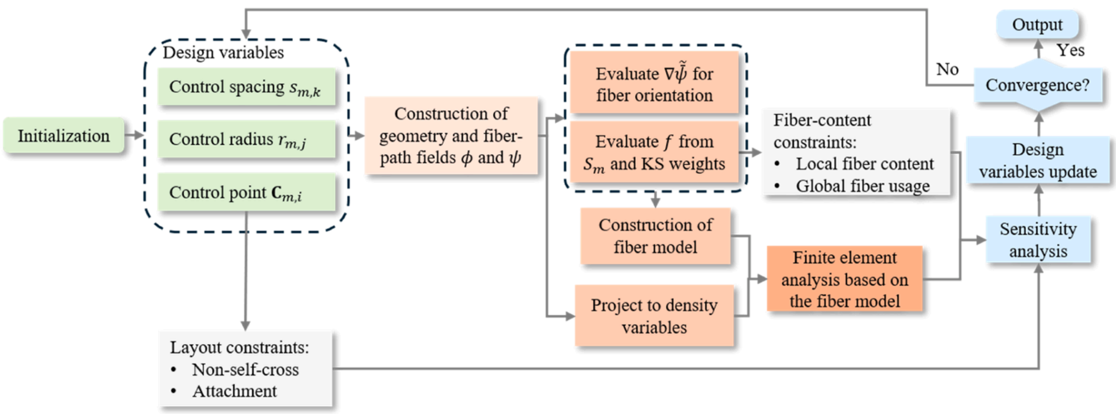

Fig. 5. Flowchart of the proposed method.

imposed fiber-content constraints.

Step 4: Sensitivity analysis and design update. Sensitivities of the objective and constraints are evaluated, and the design variables are updated using the Method of Moving Asymptotes (MMA) [74]. The process is repeated until convergence, yielding the optimized structure and printable fiber paths.

4. Numerical examples

This section presents numerical examples to demonstrate the effectiveness of the proposed framework. The examples examine the initialization strategy, manufacturability constraints, fiber-content control, and applications to both stiffness-oriented and compliant-mechanism design problems. All computations are performed on a 12-core desktop workstation with an Intel® Xeon® W-2195 CPU at 2.30 GHz, and the algorithm is implemented in MATLAB.

4.1. Parameter setting

Unless otherwise specified, the following parameter settings are adopted throughout numerical examples, and all examples are carried out in a dimensionless setting. The distance-scaling factor γ is set to 10. For each B-spline component, the radius control variables are initialized as $r_{m,j}$=0.3 with bounds $r_{m,j}\in[0.1,1]$, and the spacing control variables are initialized as $s_{m,k}$=0.5 with bounds $s_{m,k}\in[0.01,1]$. The B-spline degrees for the centerline, radius, and spacing fields are set to $p_{\mathrm{p}} = p_{\mathrm{r}} = p_{\mathrm{s}} = 3$, the numbers of centerline control points, radius control points, and spacing control points are all set to $n_{\mathrm{p}} = n_{\mathrm{r}} = n_{\mathrm{s}} = 8$.

For the non-self-crossing constraint, N_{seg}=10 sampling points are used on each control-polygon segment. The minimum clearance is defined in terms of the mesh size as $d_{\min}$=3h, where h denotes the background mesh size. For the attachment constraint, N_{att}=20 samples are taken along each B-spline centerline, and the tangent-alignment threshold is set to 20°. The target attachment distance is initialized as d_{att}=0.7 to suppress early attraction and is reduced by a factor of 1.5 every 30 iterations only when the attachment constraint is sufficiently satisfied. This continuation strategy allows the centerlines to evolve freely at the early stage and progressively promotes smooth merging of nearby trajectories. The local maximum bound and global usage limit are set to f_0=0.5 and V_{f}=1, respectively.

In the interpolation, the penalization exponent is set to p=3. For the smoothed Heaviside projection, the smoothing width is Δ=10^{-1} and the residual parameter is α=10^{-9}, During optimization, Δ is multiplied by 0.9 every 50 iterations. The KS aggregation parameter is β=128, and the p-norm exponent used in the local fiber-content constraint is $p_{\mathrm{n}} = 40$. The optimization is terminated when all constraints are satisfied and the relative change in the objective function remains below 10^{-3} for 10 consecutive iterations after the minimum iteration number of 180 is reached, or when the maximum number of 300 iterations is reached.

In all numerical examples, the physical design domain is embedded in a slightly larger auxiliary computational domain to avoid truncation of the extracted fiber paths near physical boundaries. No padding is introduced along symmetry boundaries, since they represent artificial cuts of the full structure and the fiber paths remain continuous after mirror reflection. The padding elements are treated as passive elements and are excluded from the volume constraint and structural performance evaluation. In this work, a padding width of 0.1 is used to prevent boundary truncation while avoiding unnecessary computational cost.

The fiber phase is modeled as an orthotropic material, while the matrix phase is assumed to be isotropic. The corresponding material parameters are summarized in Table 1.

4.2. MBB beam

As shown in Fig. 6(a), the MBB beam benchmark is defined on a 4.2×1.2 rectangular domain, with a centered 4.0×1.0 design region surrounded by a 0.1-thick non-design layer. The beam is simply supported at the two bottom corners and loaded by a unit downward point force at the midpoint of the top boundary. Due to symmetry in both geometry and loading, only the right half is optimized, with symmetry boundary conditions imposed along the vertical centerline. The domain is discretized into 220×140 bilinear quadrilateral elements, and the prescribed volume fraction is 0.5.

4.2.1. Initialization strategy

In geometry-driven topology optimization frameworks, the optimized layouts may exhibit notable sensitivity to the initial configuration of geometric descriptors. This effect is particularly pronounced in CFRCs design, where the initial fiber architecture plays a critical role in shaping the optimization trajectory. Similar behavior has also been observed in other topology optimization paradigms [55,62], where different initial geometric or orientation fields can lead to convergence toward distinct local optima. Accordingly, this subsection examines the impact of initialization and proposes a physically informed strategy to improve robustness and performance.

To alleviate this sensitivity, it is desirable to incorporate mechanics-based priors into the initialization process. In fiber-reinforced

Table 1
Material parameters.

Materials	E_1	E_1	ν_{12}	G_{12}
Fiber	69.4	5.5	0.33	1.9
Matrix	4.76	4.76	0.37	1.74

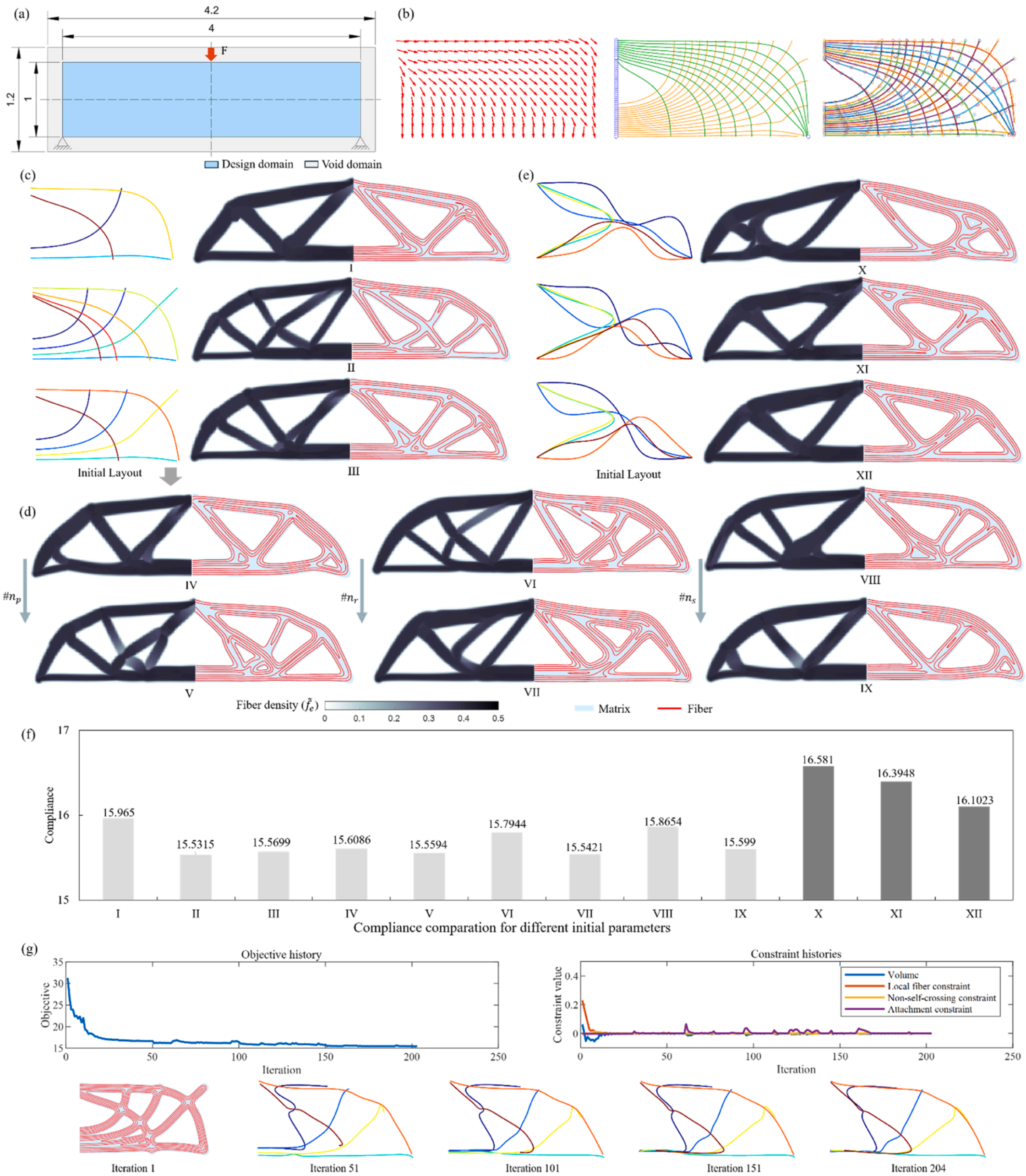

Fig. 6. MBB beam benchmark and initialization study. (a) Boundary conditions. (b) Principal-stress-based initialization strategy. (c) Optimized structures obtained with different numbers of B-spline components: **I**. $(\boldsymbol{M}, \boldsymbol{n}_\mathbf{p}, \boldsymbol{n}_\mathbf{r}, \boldsymbol{n}_\mathbf{s}) = (4,8,6,6)$, **II**. $(\boldsymbol{M}, \boldsymbol{n}_\mathbf{p}, \boldsymbol{n}_\mathbf{r}, \boldsymbol{n}_\mathbf{s}) = (8,8,6,6)$, **III**. $(\boldsymbol{M}, \boldsymbol{n}_\mathbf{p}, \boldsymbol{n}_\mathbf{r}, \boldsymbol{n}_\mathbf{s}) = (6,8,6,6)$. (d) Optimized structures obtained with different initial parameter settings: **IV**. $(\boldsymbol{M}, \boldsymbol{n}_\mathbf{p}, \boldsymbol{n}_\mathbf{r}, \boldsymbol{n}_\mathbf{s}) = (6,6,6,6)$, **V**. $(\boldsymbol{M}, \boldsymbol{n}_\mathbf{p}, \boldsymbol{n}_\mathbf{r}, \boldsymbol{n}_\mathbf{s}) = (6,10,6,6)$, **VI**. $(\boldsymbol{M}, \boldsymbol{n}_\mathbf{p}, \boldsymbol{n}_\mathbf{r}, \boldsymbol{n}_\mathbf{s}) = (6,8,4,6)$, **VII**. $(\boldsymbol{M}, \boldsymbol{n}_\mathbf{p}, \boldsymbol{n}_\mathbf{r}, \boldsymbol{n}_\mathbf{s}) = (6,8,8,6)$, **VIII**. $(\boldsymbol{M}, \boldsymbol{n}_\mathbf{p}, \boldsymbol{n}_\mathbf{r}, \boldsymbol{n}_\mathbf{s}) = (6,8,6,4)$, **IX**. $(\boldsymbol{M}, \boldsymbol{n}_\mathbf{p}, \boldsymbol{n}_\mathbf{r}, \boldsymbol{n}_\mathbf{s}) = (6,8,6,8)$. (e) Optimization results obtained using the initialization procedure suggested by Zhu et al. [66]. (f) Comparison of the compliance values. (g) Objective and constraint convergence histories for case V.

structural design, aligning fibers with principal stress directions is well known to promote efficient load transfer and enhance stiffness. Building on this principle, a stress-streamline-based initialization strategy is adopted. As illustrated in Fig. 6(b), the procedure consists of three steps: (i) initializing the design domain as fully solid and performing finite element analysis to obtain the stress field; (ii) extracting principal-stress streamlines and selecting those seeded from the fixed boundary and loading regions to construct a physically informed initial layout; and (iii) generating control points of each B-spline component via equal-arc-length sampling along the selected streamlines.

To further assess the sensitivity of the proposed initialization, the B-spline construction parameters M, n_p, n_r, and n_s are systematically varied. The optimized designs and corresponding compliance values shown in Fig. 6(c) and (d) range from 15.5315 to 15.9650. Among all cases, the configuration with the largest number of curves (M=8, Case II) achieves the lowest compliance, whereas that with the fewest curves (M=4, Case I) yields the highest compliance.

Parametric study also highlights the distinct roles of these parameters. Increasing M improves the coverage of dominant stress-transfer regions and enriches the set of admissible load paths, generally reducing compliance, although excessively large M may introduce redundant trajectories and increase computational cost. The parameter n_p controls the geometric flexibility of each B-spline curve; larger n_p enables more accurate representation of curved trajectories and tends to improve performance. The parameter n_r governs the spatial variation of the influence radius along each trajectory and thus affects effective member thickness, while larger n_r allows smoother thickness transitions. Finally, n_s determines the resolution of the fiber-density field and increasing n_s enables more adaptive reinforcement allocation along the trajectories, thereby further reducing compliance.

For comparison, Fig. 6(e) adopts the initialization strategy proposed by Zhu et al. [66], where the curve endpoints are fixed and the intermediate control points are randomly generated. In the present framework, this strategy does not yield consistent solutions, because the initial B-spline geometry directly determines the induced fiber-path field and the corresponding initial fiber directions. Consequently, different random centerlines lead to different local optima. Moreover, the resulting compliance values are all higher than those obtained using the proposed initialization strategy.

It should be noted that stress-streamline-based initialization is mainly suitable for single-load-case stiffness-oriented problems. For multiple-load-case problems, conflicting principal stress fields may introduce initialization bias if only one stress field is used. As noted by Zhao [75], optimized fiber orientations in multiple-load-case CFRC topology optimization are not necessarily aligned with principal stress directions in all elements. Possible extensions include aggregated stress fields, load-case-dependent initial components, or multi-start initialization to improve robustness.

The convergence behavior is illustrated in Fig. 6(g) using Case V as a representative example. The objective function decreases rapidly in the early iterations and then gradually stabilizes. Meanwhile, the volume, local fiber-content, non-self-crossing, and attachment constraints are progressively controlled within admissible levels. Although small fluctuations occur during the continuation update of parameters, all constraints eventually stabilize, demonstrating the stable convergence of the proposed optimization procedure.

4.2.2. Effect of the manufacturability constraints

This section examines the effects of the proposed manufacturability constraints on the optimized layouts and continuous fiber paths, particularly in terms of geometric regularity, continuity, and manufacturability. As shown in Fig. 7(a), all studies in this section are conducted using the same initial B-spline layout.

Fig. 7(a) illustrates how the lower bound on the component radius $r_{\min}$, controls the geometric length scale of the optimized layout. With γh=0.05, $r_{\min}$=0.1 corresponds to a minimum member diameter of $2r_{\min}$=0.2, approximately four elements, as highlighted by the red circle. As $r_{\min}$ increases from 0.1 to 0.3, this chord becomes progressively thicker, demonstrating the expected length-scale regularization effect. When $r_{\min}$=0.4, the implied minimum diameter $2r_{\min}$=0.8 (16 elements) becomes comparable to the local spacing between neighboring members near the support, causing the chord to merge with adjacent members into a thicker fused load path.

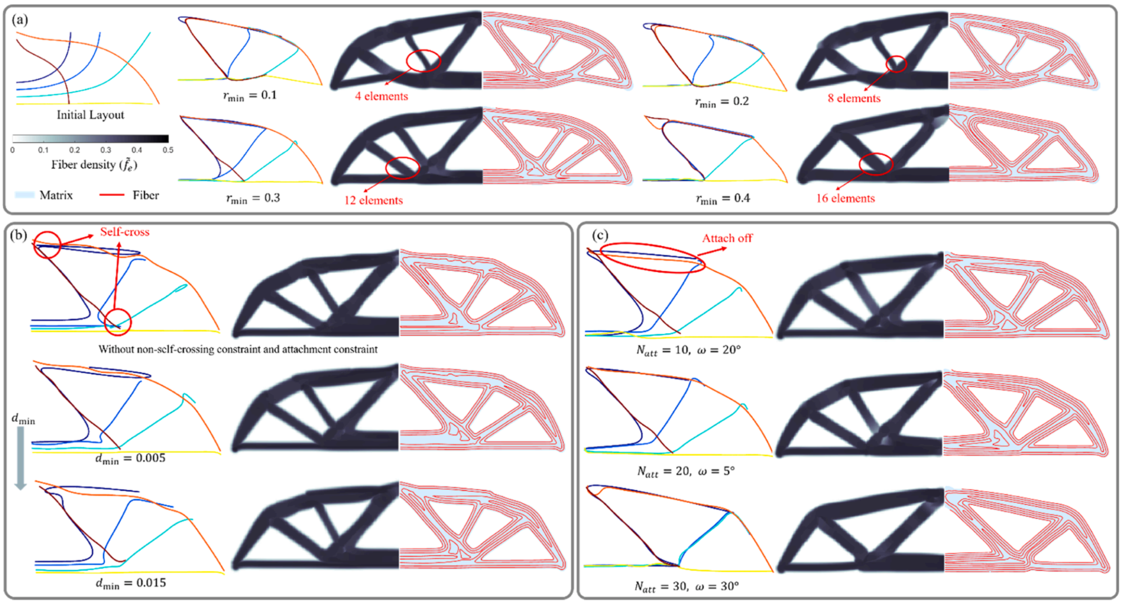

Fig. 7. Effect of the proposed manufacturability constraints. (a) Length-scale control through the lower bound on the radius variables $\boldsymbol{r}_{m,j}$. (b) Non-self-crossing constraint under different minimum-distance settings. (c) Attachment constraint under different parameter settings.

Fig. 7(b) compares the results without and with the proposed non-self-crossing constraint and illustrates the effect of the minimum separation distance $d_{\min}$. Without the non-self-crossing constraint, several B-spline trajectories intersect in the region highlighted by the red circle, leading to crowded fiber paths, ambiguous local orientations, and disturbed fiber-content distributions. When the non-self-crossing constraint is imposed, these intersections are progressively suppressed by enforcing a minimum distance between neighboring trajectories. A small value ($d_{\min} = 0.005$) removes most crossings but still allows local bundling, whereas larger values ($d_{\min} = 0.015$) produce increasingly clearer and more regularized fiber layouts.

Fig. 7(c) evaluates the effectiveness of the attachment constraint. As observed from the cases without the attachment constraint in Fig. 7(b), local drifting and weak coherence between neighboring trajectories may lead to crossings, ambiguous orientations, and

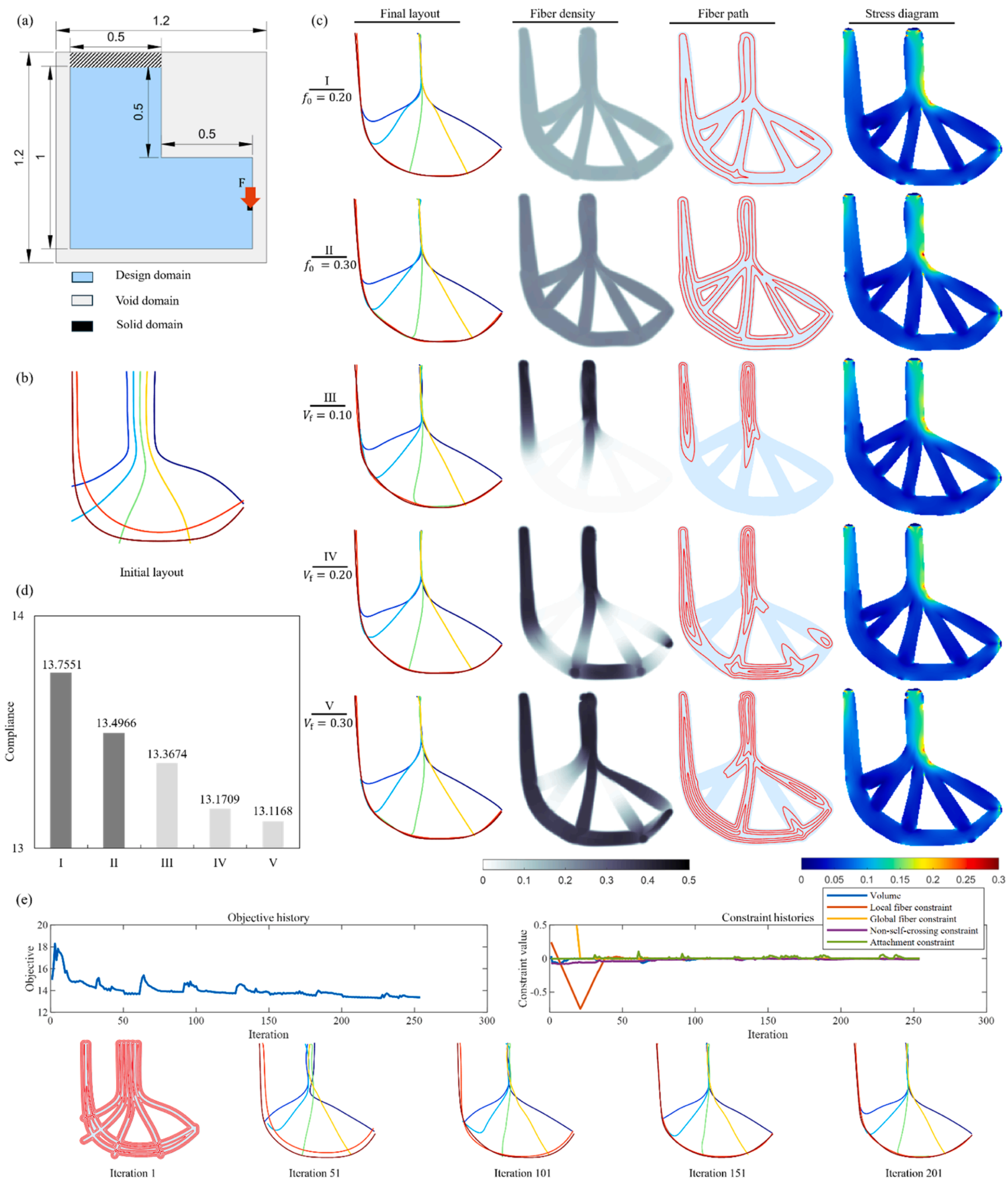

Fig. 8. L-bracket benchmark and the effect of fiber-content constraints. (a) Boundary conditions. (b) Initial B-spline component layout. (c) Optimized results under different local maximum fiber-density bounds and global fiber-volume-fraction constraints. From left to right, the columns show the optimized B-spline layouts, structural designs, generated continuous fiber paths, and stress distributions. (d) Comparison of the compliance values. (e) Objective and constraint convergence histories for Case III.

uneven path spacing. When the attachment constraint is imposed, a small sampling number, such as N_{att}=10, may still leave some isolated segments insufficiently coupled, as highlighted by the red circles. Increasing N_{att} from 10 to 20 improves the detection of neighboring segments requiring attachment and reduces these uncoupled regions. The angle threshold ω controls the selectivity of attachment. When ω is too small, e.g., ω=5° only nearly parallel segments are allowed to attach, and visible branching may remain even with a larger N_{att}. Increasing both N_{att} and ω, e.g., N_{att}=30 and $\omega = 30°$, promotes stronger merging between neighboring B-spline trajectories, thereby reducing branching. Therefore, N_{att} and ω should be selected to balance path coherence and geometric diversity.

4.3. L-bracket

The L-bracket benchmark is defined on a 1.2×1.2 square computational domain. A surrounding frame of thickness 0.1 is prescribed as a non-design region. The design region has an L-shaped geometry obtained by removing a 0.5×0.5 square from the upper-right corner, creating a corner that is prone to stress concentration. A clamped boundary condition is imposed on the hatched support segment along the top-left edge, with a support length of 0.5. A unit vertical downward load is applied at the mid-point of the right boundary. To mitigate numerical stress singularity, the load is distributed over a short boundary segment spanning five elements, as indicated in Fig. 8(a). The computational domain is discretized using 240×240 bilinear quadrilateral elements. The prescribed volume fraction is set to 0.5 with respect to the design domain, and the initial B-spline layout is shown in Fig. 8(b).

Fig. 8(c), Cases I and II, illustrate the influence of the local upper bound f_0 on the maximum fiber density and its effect on the optimized layout and resulting fiber paths. When $f_0 = 0.20$, the local cap is restrictive and limits the admissible reinforcement level, resulting in comparatively sparse fiber trajectories and the highest compliance among the considered cases ($c = 13.7551$). Increasing the bound to $f_0 = 0.3$ relaxes the local constraint and permits a higher reinforcement level within the structure. Consequently, the

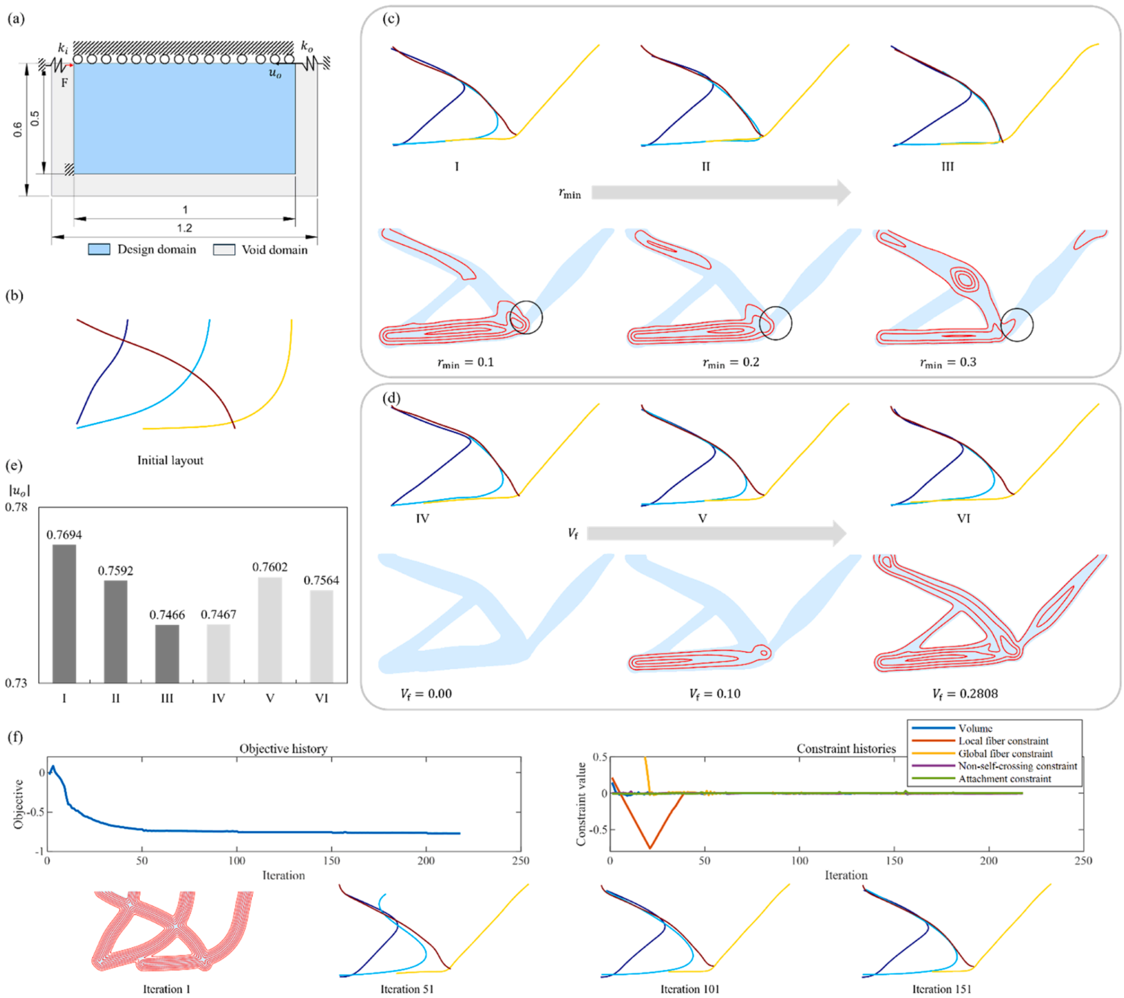

Fig. 9. Compliant mechanism benchmark. (a) Boundary conditions. (b) Initial B-spline component layout. (c) Effect of the minimum radius $\boldsymbol{r}_{\mathbf{min}}$. (d) Effect of different fiber-content settings with $\boldsymbol{r}_{\mathbf{min}} = 0.1$. (e) Comparison of the absolute output displacements $|\boldsymbol{u}_{\mathbf{o}}|$. (f) Objective and constraint convergence histories for Case V.

compliance decreases to $c = 13.4966$, corresponding to a total reduction of 1.88% relative to the case with $f_0 = 0.20$.

Fig. 8(c), Cases III–V, examines the influence of the global fiber-usage limit by varying the allowable fiber budget V_f. When $V_\mathrm{f} = 0.10$, the fiber density remains low over most of the structure, and the extracted fiber paths are mainly concentrated in the most critical load-bearing regions. As V_f increases, reinforcement is progressively expanded and densified along the dominant stress-transfer paths and around highly stressed junctions. Correspondingly, the compliance decreases monotonically from $c = 13.1709$ at $V_\mathrm{f} = 0.20$ to $c = 13.1168$ at $V_\mathrm{f} = 0.30$, corresponding to an overall improvement of about 0.41%. These results show that the proposed formulation uses the available fiber budget in a mechanically meaningful way and enables a clear trade-off between fiber usage and structural performance.

It should be noted that the L-bracket may admit more stiffness-efficient layouts in an unrestricted density-based or level-set-based design space. In the present framework, the design space is restricted by the finite B-spline component representation and manufacturability-related constraints, including continuous-path generation, component attachment, non-self-crossing control, and fiber-content regulation. Therefore, the optimized L-bracket designs should be interpreted as manufacturable local optima within the proposed B-spline component-based design space. Compared with previous studies reporting highly localized fiber concentration near the re-entrant corner [76], Fig. 8(c) shows smoother material and fiber-path redistribution around the corner. This reflects a trade-off between compliance performance and manufacturable continuous fiber-path regularity.

The convergence histories of Case III are shown in Fig. 8(e). The objective function decreases and gradually stabilizes, while the volume, local/global fiber-content, non-self-crossing, and attachment constraints remain controlled within admissible levels. This confirms that the proposed formulation achieves stable convergence while regulating fiber usage in the L-bracket benchmark.

4.4. Compliant mechanism

In this section, compliant mechanism design problems are considered to further demonstrate the applicability of the proposed method. The design domain is illustrated in Fig. 9(a), where only the bottom half is shown due to symmetry. The benchmark is defined on a 1.2×0.6 rectangular computational domain. A surrounding frame of thickness 0.1 is prescribed as a non-design region, except along the symmetry boundary. The bottom-left corner is fixed, and a unit input load is applied at the upper-left input port. The objective is to maximize the output displacement u_o at the upper-right corner. Two springs with stiffnesses k_i=0.5 and k_o=0.1 are attached to the input and output ports, respectively. The maximum allowable material usage is set to 0.3. The domain is discretized using 240×120 bilinear quadrilateral elements, and the initial B-spline layout is shown in Fig. 9(b).

Fig. 9(c) compares the optimized displacement inverter designs obtained with different minimum radius values. When $r_\mathrm{min} = 0.1$, relatively slender members are allowed, the thinnest region appears at the inclined junction highlighted by the black circle. This case achieves the best inverter performance among the three cases, with $u_o = -0.7694$. As r_min increases to 0.2, the structural members become noticeably thicker, and the magnitude of the output displacement decreases to $u_o = -0.7592$. With a further increase to $r_\mathrm{min} = 0.3$, the minimum feature-size restriction becomes stronger, leading to a bulkier layout and a further reduction in the output displacement magnitude to $u_o = -0.7466$.

Fig. 9(d) compares the optimized displacement inverter designs obtained under different fiber-content settings. Without fiber reinforcement, the output displacement is $u_o = -0.7467$. When a relatively small fiber-content bound is introduced, i.e., $V_\mathrm{f} = 0.10$, the optimized design achieves a larger output displacement of $u_o = -0.7602$. However, when the lower bound of the spacing-control variable is increased to $s_{min} = 0.2$, the fiber paths cover almost the entire structure, and the output displacement magnitude decreases to $u_o = -0.7564$. These results indicate that moderate fiber reinforcement can improve the output response of the compliant mechanism, whereas excessive reinforcement tends to over-stiffen the structure and suppress the desired deformation transmission.

The convergence histories of Case V are shown in Fig. 9(f). The objective function gradually stabilizes as the displacement-inverter layout is refined to enhance the output response. Meanwhile, the volume, local/global fiber-content, non-self-crossing, and attachment constraints remain controlled within admissible levels. This indicates that the proposed formulation can achieve stable convergence for the compliant mechanism design while balancing fiber reinforcement and deformation transmission.

5. Full-scale reconstruction and verification

This section presents full-scale reconstruction and post-optimization verification for representative designs from the preceding examples. Since topology optimization is performed using a homogenized material model, the optimized designs must be de-homogenized into full-scale models with explicit matrix and continuous-fiber regions for manufacturable realization. Several reconstructed designs are therefore examined through comparative finite-element simulations to assess the discrepancy between homogenized predictions and full-scale responses.

Due to the high computational cost, the present verification is limited to 2D cases. For future 3D applications, full-scale simulation efficiency may be improved by using GPU-accelerated finite-element solvers, matrix-free or multigrid-preconditioned iterative solvers, and efficient orientation-dependent element stiffness evaluation strategies [77,78].

5.1. Full-scale model reconstruction

By taking advantage of the specific data exported by the proposed framework, the reconstruction of CFRCs can be carried out conveniently and accurately, which also facilitates subsequent manufacturing. Each B-spline centerline can first be reconstructed in a CAD environment. The corresponding boundary curves $\mathscr{S}$ of each spline component can then be obtained as:

$$\mathscr{S}(\xi) = \mathscr{P}(\xi) \pm R(\xi) \cdot \boldsymbol{N}(\xi) \tag{48}$$

Based on this formulation, all boundary curves can be generated in CAD, as shown in Fig. 10(a). After removing the redundant internal curves, only the structural boundaries are retained, as shown in Fig. 10(b). For the MBB case, the reconstructed boundary is mirrored to obtain the complete MBB beam, as shown in Fig. 10(c). In this way, the geometry of the optimized result is preserved to the greatest extent. Subsequently, the fiber paths obtained from the de-homogenization process, i.e., the iso-contours of the scalar field, are then imported into the CAD model to form the boundary-plus-fiber-path representation shown in Fig. 10(d). The reconstructed CAD model is then imported into COMSOL Multiphysics 6.4 for full-scale simulation.

In many existing full-scale CFRC simulations, the fiber-path orientation is neglected, and both matrix and fiber regions are modeled using equivalent isotropic materials, thereby ignoring the orthotropic anisotropy of fiber reinforcement. In this work, the material parameters are kept consistent with those in Table 1, with elastic moduli given in GPa. The direction orthogonal to the scalar-field gradient is imported as the fiber-orientation field, ensuring consistency between the full-scale simulation and the optimization model. A finite fiber thickness of 1 mm is assigned, as illustrated in Fig. 10(e), and the full model is discretized using a free triangular mesh.

5.2. *Comparison of fiber-path layouts in the MBB beam*

Using the structure shown in Fig. 6(d), Case V, as an example, this section presents the reconstructed full-scale model and its corresponding simulation results. The overall dimensions of the model are 400×100 mm, while only one half of the symmetric structure is shown in the simulation results. The boundary conditions are the same as those used in Fig. 6(a), and a concentrated load of 1×10^3 kN is applied. To further demonstrate the importance of fiber-path design in CFRCs, two simple reference models with uniformly distributed horizontal and vertical fiber paths, together with a boundary-offset model taken as a sequential post-processing baseline in which the fiber paths are generated by inward offset of the structural boundary, are considered under the same structural geometry, as summarized in Table 2. For a fair comparison, the total fiber lengths of the four models are kept nearly identical, being 6560.9, 6517.1, 6576.3, and 6548.6 mm for the optimized-path, horizontal-path, vertical-path, and boundary-offset models, respectively.

For all four models, the maximum displacement occurs near the central loading point. The optimized-path model gives the smallest maximum displacement (2.67 mm), compared with 3.31, 3.95, and 3.45 mm for the horizontal-path, vertical-path, and boundary-offset models, respectively, corresponding to reductions of 19.34%, 32.41%, and 22.61%. The corresponding average displacements are 1.38, 1.66, 2.00, and 1.94 mm, giving reductions of 16.87%, 31.00%, and 28.87%, respectively. Among the reference cases, the vertical-path model performs worst because its fiber trajectories are poorly aligned with the dominant inclined load-transfer paths, while the boundary-offset model, although more meaningful as a sequential baseline, still cannot adapt the fiber layout effectively to the internal stress-transfer mechanism. Overall, these full-scale results show that the proposed B-spline-driven optimization strategy is more effective than both simple preset layouts and boundary-offset-based post-processing in enhancing the stiffness of CFRCs.

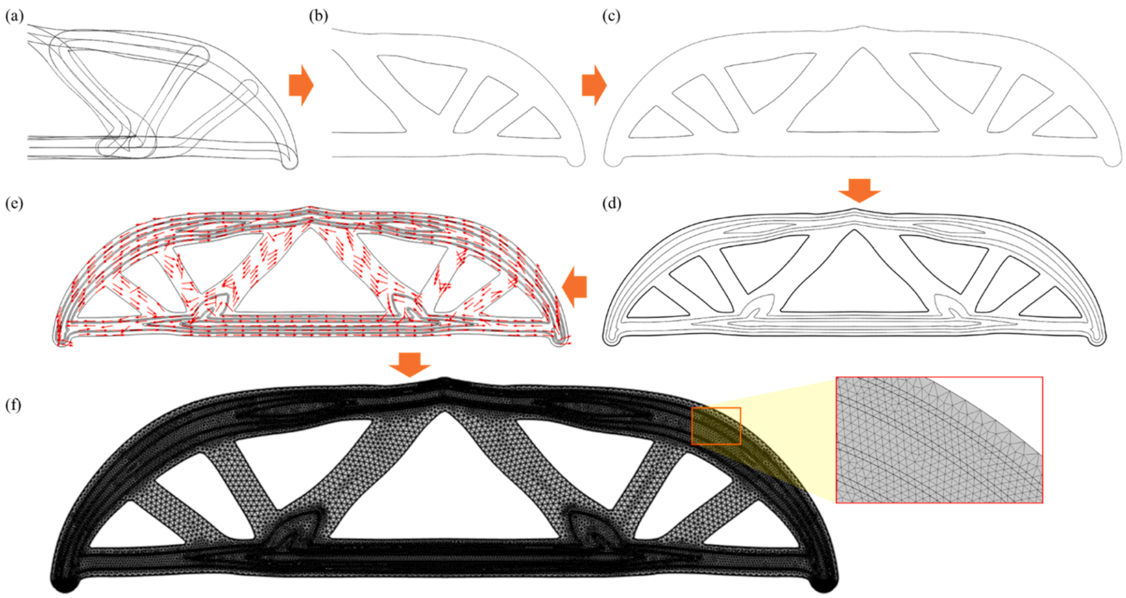

Fig. 10. Full-scale reconstruction process of the optimized MBB beam. (a) Generation of the B-spline boundary curves. (b) Removal of redundant curves to retain only the structural boundaries. (c) Symmetry completion of the half model to obtain the full MBB beam. (d) Import of the de-homogenized fiber paths. (e) Import into COMSOL, assignment of fiber thickness and fiber orientation. (f) Free-triangular meshing of the reconstructed CFRCs model.

Table 2
Comparison of reconstructed full-scale CFRC MBB beam models with optimized, horizontal, vertical, and boundary-offset fiber-path layouts in terms of total fiber length, maximum displacement, and average displacement.

Fiber path	Optimized path	Horizontal path	Vertical path	Boundary offset
Models for analysis	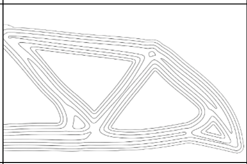	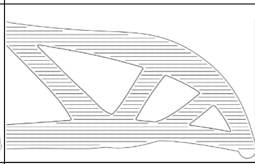	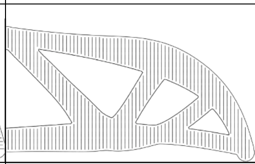	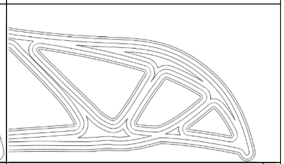
Total.disp (mm)	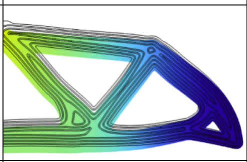	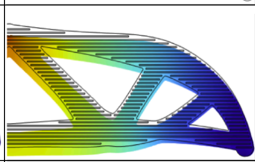	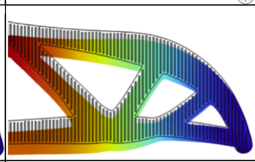	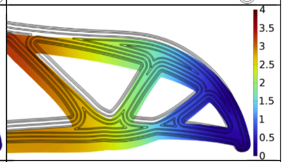
Total fiber length (mm)	6560.9	6517.1	6576.3	6548.6
Max.disp (mm)	2.67	3.31	3.95	3.45
Ave.disp (mm)	1.38	1.66	2.00	1.94

5.3. Comparison of fiber-usage strategies in the compliant mechanism

To further examine the influence of fiber reinforcement at the full-scale reconstruction level for the compliant mechanism problem, three representative cases from Fig. 9(d) (Cases IV, V, and VI) are compared in this section. The reconstructed model has overall dimensions of 240 × 240 mm, and the full response is obtained from the half model by symmetry. The boundary conditions are the

Table 3
Comparison of reconstructed CFRC compliant mechanism models for three design strategies: without fiber reinforcement, with fiber-usage limitation, and with a minimum fiber-density.

Fiber path	Without fiber reinforcement	With a fiber-usage limit ($V_f = 0.10$)	With a minimum fiber-density
Models for analysis	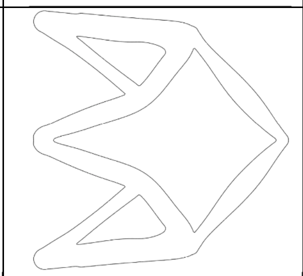	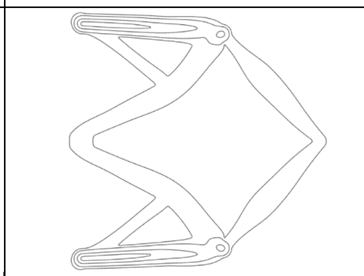	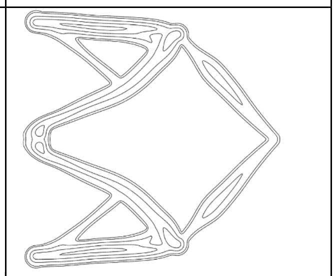
Total.disp (mm)	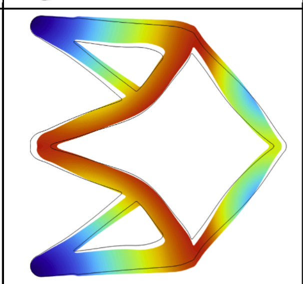	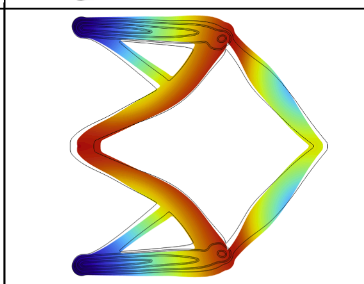	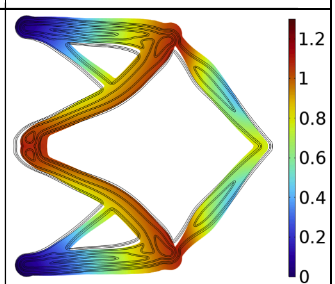
Total fiber length (mm)	0	1319.9	3757.2
Out.disp (mm)	0.7465	0.7649	0.7566

same as those in Fig. 9(a).

As shown in Table 3, the case without fiber reinforcement yields an output displacement of 0.7465 mm. When fiber reinforcement is introduced with a fiber-usage limit of $V_{\mathrm{f}} = 0.10$, the total fiber length is 1319.9 mm, and the output displacement increases to 0.7649 mm, corresponding to an improvement of 2.46%. By contrast, when a minimum fiber-density constraint is further imposed, the total fiber length increases substantially to 3757.2 mm, while the output displacement decreases to 0.7566 mm. These results indicate that moderate fiber reinforcement can enhance the output performance, whereas excessive fiber coverage tends to over-stiffen the structure and hinder the deformation transmission required for compliant motion. Therefore, unlike stiffness-dominated structural design, compliant mechanism design requires a more delicate balance between local reinforcement and global flexibility.

6. Conclusion

This paper presents a B-spline-driven topology and fiber-path optimization framework for additively manufactured CFRCs. The structural geometry is modeled using multiple variable-width B-spline components. Based on the same component representation, a fiber-path scalar field is introduced so that continuous fiber paths can be generated through iso-contour extraction, while an additional spacing-control field enables spatially varying path spacing and reinforcement allocation. In addition, manufacturability-related constraints, including the non-self-crossing constraint, the attachment constraint, and fiber-content constraints, are incorporated to improve path regularity, regulate reinforcement allocation, and enhance printability.

The numerical results show that the proposed non-self-crossing constraint prevents irregular or degenerate distributions of B-spline centerlines, thereby ensuring smooth and physically meaningful fiber-path layouts, whereas the attachment constraint improves the geometric coherence among neighboring components and leads to clearer skeleton-based structural representations. Meanwhile, the minimum feature size can be directly controlled through the lower bound on the radius variables. In addition, the introduced fiber-content constraints enable both local adjustment of fiber spacing and global regulation of fiber usage, allowing flexible and targeted reinforcement allocation. For compliant-mechanism design, the results further indicate that moderate fiber reinforcement can enhance the output response, whereas excessive reinforcement tends to over-stiffen the structure and suppress the desired deformation transmission. Owing to the explicit geometry-driven representation, the optimized results can also be directly converted into CAD models without requiring complex post-processing.

It should be noted that the present framework is geometry-driven: fiber paths are extracted from the scalar field induced by the B-spline components rather than independently parameterized. This coupling improves path continuity, geometric interpretability, and CAD compatibility, but limits independent fiber-path design freedom. Future work will introduce additional path-level design variables and more explicit process-specific manufacturing constraints, including curvature bounds, minimum turning-radius constraints, start/stop rules, and collision or overlap handling. The computational efficiency can also be improved using acceleration techniques such as the template stiffness matrices (TSMs)-based method for Cartesian-grid CFRC topology optimization [75]. In addition, the framework will be extended to 3D settings, and experimental validation using printed CFRC specimens will be pursued.

CRediT authorship contribution statement

Yifan Guo: Writing – original draft, Visualization, Validation, Methodology, Conceptualization. **Jikai Liu:** Writing – review & editing, Supervision, Conceptualization. **Shuzhi Xu:** Writing – review & editing, Supervision, Methodology, Investigation, Conceptualization. **Kentaro Yaji:** Writing – review & editing, Methodology, Conceptualization. **Takayuki Yamada:** Writing – review & editing, Supervision, Methodology, Investigation, Funding acquisition, Conceptualization.

Declaration of competing interest

The authors declare that they have no known competing financial interests or personal relationships that could have appeared to influence the work reported in this paper.

Acknowledgements

This work was supported in part by JSPS KAKENHI Grant Numbers JP23H03800, JP25H01108, and 25KF0244.

Appendix

This appendix presents the first-order derivatives required by the MMA optimizer for the objective and constraints.

A.1. Sensitivity of the objective function

For any scalar design variables λ, the sensitivity of the objective function takes different forms for the compliance and compliant mechanism objectives, given by:

$$\begin{cases} \dfrac{\partial c}{\partial \lambda} = -\mathbf{U}^T \dfrac{\partial \mathbf{K}}{\partial \lambda} \mathbf{U} = -\displaystyle\sum_{e=1}^{N_e} \mathbf{u}_e^T \dfrac{\partial \mathbf{K}_e}{\partial \lambda} \mathbf{u}_e, & \text{Compliance} \\ \dfrac{\partial c}{\partial \lambda} = \mathbf{P}^T \dfrac{\partial \mathbf{K}}{\partial \lambda} \mathbf{U} = \displaystyle\sum_{e=1}^{N_e} \mathrm{p}_e^T \dfrac{\partial \mathbf{K}_e}{\partial \lambda} \mathbf{u}_e, & \text{Compliant mechanism} \end{cases} \tag{49}$$

For the compliant mechanism objective, the adjoint vector **P** is obtained from the following adjoint equation:

$$\mathbf{KP} = \mathbf{L} \tag{50}$$

where **L** is the output selection vector. With the SIMP method from Eq. (23), $\frac{\partial \mathbf{K}_e}{\partial \lambda}$ yields:

$$\frac{\partial \mathbf{K}_e}{\partial \lambda} = \frac{\partial \rho_e^p}{\partial \lambda} \int_{\Omega_e} \mathbf{B}^T \mathbf{D}_{e,\theta}^0 \mathbf{B} \mathrm{d}\Omega + \rho_e^p \int_{\Omega_e} \mathbf{B}^T \frac{\partial \mathbf{D}_{e,\theta}^0}{\partial \lambda} \mathbf{B} \mathrm{d}\Omega. \tag{51}$$

The density term $\frac{\partial \rho_e^p}{\partial \lambda}$ is:

$$\frac{\partial \rho_e^p}{\partial \lambda} = p \rho_e^{p-1} \frac{\partial \rho_e}{\partial \lambda}, \quad \frac{\partial \rho_e}{\partial \lambda} = \frac{\partial \widetilde{H}(\phi)}{\partial \lambda} = \frac{\partial \widetilde{H}(\phi)}{\partial \phi} \frac{\partial \phi}{\partial \lambda}, \tag{52}$$

where $\frac{\partial \phi}{\partial \lambda}$ can be calculated by chain rule:

$$\frac{\partial \phi}{\partial \lambda} = \sum_{m=1}^{M} \frac{\partial \phi}{\partial \phi_{m,e}} \frac{\partial \phi_{m,e}}{\partial \lambda}. \tag{53}$$

$\frac{\partial \phi}{\partial \phi_{m,e}}$ is the KS aggregation weight, and $\frac{\partial \phi_{m,e}}{\partial \lambda}$ can be given by:

$$\frac{\partial \phi_{m,e}}{\partial \lambda} = \frac{\partial R_m(\Xi_{m,e})}{\partial \lambda} - \gamma \frac{\partial D_{m,e}(\boldsymbol{x}_e)}{\partial \lambda}, \tag{54}$$

where $\frac{\partial R_m(\Xi_{m,e})}{\partial \lambda}$ is derived from Eq. (2):

$$\frac{\partial R_m(\Xi_{m,e})}{\partial \lambda} = \sum_{j=1}^{n_r} \mathscr{B}_j(\Xi_{m,e}) + \left(\sum_{j=1}^{n_r} \mathscr{B}_j^{'}(\Xi_{m,e}) r_{m,j} \right) \frac{\partial \Xi_{m,e}}{\partial \mathbf{C}_{m,i}}. \tag{55}$$

The derivative $\frac{\partial \Xi_{m,e}}{\partial \mathbf{C}_{m,i}}$ is obtained by differentiating the closest-point optimality condition using the implicit function theorem, resulting in:

$$\frac{\partial \Xi_{m,e}}{\partial \mathbf{C}_{m,i}} = -\frac{\mathscr{B}_i(\Xi_{m,e}) \mathscr{P}_m^{'}(\Xi_{m,e}) + \mathscr{B}_i^{'}(\Xi_{m,e}) \left(\mathscr{P}_m(\Xi_{m,e}) - \boldsymbol{x}_e \right)}{\mathscr{P}_m^{'}(\Xi_{m,e})^T \mathscr{P}_m^{'}(\Xi_{m,e}) + \left(\mathscr{P}_m(\Xi_{m,e}) - \mathbf{x}_e \right)^T \mathscr{P}_m^{''}(\Xi_{m,e})}. \tag{56}$$

Here,

$$\mathscr{P}_m^{'}(\Xi) = \sum_{i=1}^{n_p} \mathscr{B}_i^{'}(\Xi) \mathbf{C}_{m,i} \ , \ \mathscr{P}_m^{'}(\Xi) = \sum_{i=1}^{n_p} \mathscr{B}_i^{''}(\Xi) \mathbf{C}_{m,i}. \tag{57}$$

The distance term $\frac{\partial D_{m,e}(\boldsymbol{x}_e)}{\partial \lambda}$ in Eq. (54) is given by:

$$\frac{\partial D_{m,e}(\boldsymbol{x}_e)}{\partial \lambda} = \frac{\| \mathscr{P}_m(\Xi_{m,e}) - \boldsymbol{x}_e \|^T}{D_{m,e}} \left(\frac{\partial \mathscr{P}_m(\Xi_{m,e})}{\partial \mathbf{C}_{m,i}} + \mathscr{P}_m^{'}(\Xi_{m,e}) \frac{\partial \Xi_{m,e}}{\partial \mathbf{C}_{m,i}} \right). \tag{58}$$

For control-point coordinates:

$$\frac{\partial \mathscr{P}_m(\Xi_{m,e})}{\partial x_{m,i}} = \mathscr{B}_i(\Xi_{m,e}) [1, 0]^T, \quad \frac{\partial \mathscr{P}_m(\Xi_{m,e})}{\partial y_{m,i}} = \mathscr{B}_i(\Xi_{m,e}) [0, 1]^T. \tag{59}$$

The second term in Eq. (51) $\frac{\partial \mathbf{D}_{e,\theta}^0}{\partial \lambda}$ can use the chain rule with respect to the fiber angle and the local fiber-density indicator:

$$\frac{\partial \mathbf{D}_{e,\theta}^0}{\partial \lambda} = \frac{\partial \mathbf{D}_{e,\theta}^0}{\partial \theta_e} \frac{\partial \theta_e}{\partial \lambda} + \frac{\partial \mathbf{D}_{e,\theta}^0}{\partial f_e} \frac{\partial f_e}{\partial \lambda}, \tag{60}$$

where $\frac{\partial \mathbf{D}_{e,\theta}^0}{\partial \theta_e}$, $\frac{\partial \mathbf{D}_{e,\theta}^0}{\partial f_e}$ can refer to [73], $\frac{\partial \theta_e}{\partial \lambda}$ is derived from Eq. (17):

$$\frac{\partial\theta_e}{\partial\lambda}=\frac{\varphi_x}{\varphi_x^2+\varphi_y^2}\frac{\partial\varphi_y}{\partial\lambda}-\frac{\varphi_y}{\varphi_x^2+\varphi_y^2}\frac{\partial\varphi_x}{\partial\lambda}. \tag{61}$$

Here,

$$\frac{\partial\varphi_x}{\partial\lambda}=\frac{\partial\mathscr{H}\left(\frac{\partial\bar{\psi}}{\partial\psi}\frac{\partial\psi}{\partial\lambda}\right)}{\partial x}. \tag{62}$$

$\frac{\partial\bar{\psi}}{\partial\psi}$ can be derived from Eq. (14), and $\frac{\partial\psi}{\partial\lambda}$ is derived analogously to $\frac{\partial\phi}{\partial\lambda}$:

$$\frac{\partial\psi}{\partial\lambda}=\sum_{m=1}^{M}\frac{\partial\psi}{\partial\psi_{m,e}}\frac{\partial\psi_{m,e}}{\partial\lambda}\ ,\ \frac{\partial\psi_{m,e}}{\partial\lambda}=\frac{\partial\phi_{m,e}}{\partial\lambda}S_{m,e}+\phi_{m,e}\frac{\partial S_{m,e}}{\partial\lambda}, \tag{63}$$

and $\frac{\partial S_{m,e}}{\partial\lambda}$ follows the same derive process as $\frac{\partial R_{m,e}}{\partial\lambda}$. Then, $\frac{\partial f_e}{\partial\lambda}$ is derived from Eq. (19):

$$\frac{\partial f_e}{\partial\lambda}=\sum_{m=1}^{M}\left(S_{m,e}\frac{\partial w_{m,e}}{\partial\lambda}+w_{m,e}\frac{\partial S_{m,e}}{\partial\lambda}\right), \tag{64}$$

where the sensitivity of the KS ownership weight is:

$$\frac{\partial w_{m,e}}{\partial\lambda}=\beta w_{m,e}\left(\frac{\partial\psi_{m,e}}{\partial\lambda}-\sum_{i=1}^{M}w_{i,e}\frac{\partial\psi_{i,e}}{\partial\lambda}\right). \tag{65}$$

A.2. Sensitivity of the non-self-crossing constraint

The non-self-crossing constraint is imposed on the sampled points along the control polygon. Using KS aggregation over admissible pairs $(a,b)\in\mathscr{A}_m$, the derivative with respect to a control point $\mathbf{C}_{m,i}$ is:

$$\frac{\partial g_m^{\text{self}}}{\partial\mathbf{C}_{m,i}}=\sum_{(i,j)\in\mathscr{A}_m}\frac{\partial g_m^{\text{self}}}{\partial v_{ij}}\frac{\partial v_{ij}}{\partial\mathbf{C}_{m,i}}, \tag{66}$$

where $\frac{\partial g_m^{\text{conn}}}{\partial v_{ij}}$ is the KS aggregation weight, and $\frac{\partial v_{ij}}{\partial\mathbf{C}_{m,i}}$:

$$\frac{\partial v_{ij}}{\partial\mathbf{C}_{m,i}}=\left(\frac{\partial\mathbf{p}_j}{\partial\mathbf{C}_{m,i}}-\frac{\partial\mathbf{p}_i}{\partial\mathbf{C}_{m,i}}\right)^T\frac{\mathbf{p}_i-\mathbf{p}_j}{d_{ij}}. \tag{67}$$

$\frac{\partial\mathbf{p}}{\partial\mathbf{C}_{m,i}}$ is given by the linear interpolation weights on the sampled control-polygon segment.

A.3. Sensitivity of the attachment constraint

Neglecting radius sensitivities and retaining only the geometric contribution through the control points, the derivative of the attachment constraint is:

$$\frac{\partial g_m^{\text{conn}}}{\partial\mathbf{C}_{m,i}}=\frac{1}{N_{\text{att}}}\sum_{z=1}^{N_{\text{att}}}\sum_{n\neq m}\frac{\partial g_{m,z}}{\partial\mathbf{C}_{m,i}},\ \frac{\partial g_{m,z}}{\partial\mathbf{C}_{m,i}}=\frac{\partial g_{m,z}}{\partial\eta_{m,n,z}}\frac{\partial\eta_{m,n,z}}{\mathbf{C}_{m,i}}. \tag{68}$$

$\frac{\partial\eta_{m,n,z}}{\mathbf{C}_{m,i}}$ can be derived by:

$$\frac{\partial\eta_{m,n,z}}{\partial\mathbf{C}_{m,i}}=\mathrm{G}_{m,n,z}\frac{\partial d_{m,n,z}}{\partial\mathbf{C}_{m,i}}+\left(d_{m,n,z}-d_{\text{att}}\right)\frac{\partial\,\mathrm{G}_{m,n,z}}{\partial\mu_{m,n,z}}\frac{\partial\mu_{m,n,z}}{\partial\mathbf{C}_{m,i}}, \tag{69}$$

where $\frac{\partial\mathrm{G}_{m,n,z}}{\partial\mu_{m,n,z}}$ is the derivation of Heaviside function, and $\frac{\partial\mu_{m,n,z}}{\partial\mathbf{C}_{m,i}}$ is defined differently for endpoint samples and interior samples. Therefore,

$$\frac{\partial\mu_{m,n,z}}{\partial\mathbf{C}_{m,i}}=\begin{cases}\dfrac{\partial\varrho_{m,n,z}}{\partial\mathbf{C}_{m,i}}, & \text{end points},\\[2ex] \dfrac{\partial\mu_{m,n,z}}{\partial\varrho_{m,n,z}}\dfrac{\partial\varrho_{m,n,z}}{\partial\mathbf{C}_{m,i}}+\dfrac{\partial\mu_{m,n,z}}{\partial\sigma_{m,n,z}}\dfrac{\partial\sigma_{m,n,z}}{\partial\mathbf{C}_{m,i}}, & \text{otherwise},\end{cases} \tag{70}$$

where $\frac{\partial\mu_{m,n,z}}{\partial\varrho_{m,n,z}}$ and $\frac{\partial\mu_{m,n,z}}{\partial\sigma_{m,n,z}}$ is the weight of KS aggregation. When only the geometric contribution through control points is considered:

$$\frac{\partial\varrho_{m,n,z}}{\partial\mathbf{C}_{m,i}}=-\frac{\partial d_{m,n,z}}{\partial\mathbf{C}_{m,i}}. \tag{71}$$

Next, $\frac{\partial d_{m,n,z}}{\partial \mathbf{C}_{m,i}}$ is given by:

$$\frac{\partial d_{m,n,z}}{\partial \mathbf{C}_{m,i}} = \left(\frac{\mathscr{P}_m(\xi_{m,z}) - \mathscr{P}_n(\xi_{n,z})}{d_{m,n,z}}\right)^T \left(\frac{\partial \mathscr{P}_m(\xi_{m,z})}{\partial \mathbf{C}_{m,i}} \frac{\partial \mathscr{P}_n(\xi_{n,z})}{\partial \mathbf{C}_{m,i}}\right), \tag{72}$$

where the first term is the standard B-spline basis mapping. For the tangent term:

$$\frac{\partial \sigma_{m,n,z}}{\partial \mathbf{C}_{m,i}} = \mathrm{sign}\left((\mathbf{t}_m)^T \mathbf{t}_n\right)\left[\left(\frac{\partial \mathbf{t}_m}{\partial \mathbf{C}_{m,i}}\right)^T \mathbf{t}_n + \mathbf{t}_m^T \left(\frac{\partial \mathbf{t}_n}{\partial \mathbf{C}_{m,i}}\right)\right]. \tag{73}$$

The unit tangent is $\mathbf{t} = \frac{\mathscr{P}'}{\|\mathscr{P}'\|}$. Hence, for any component,

$$\frac{\partial \mathbf{t}}{\partial \mathbf{C}_{m,i}} = \frac{\partial \mathbf{t}}{\partial \mathscr{P}'_m(\xi_{m,z})} \frac{\partial \mathscr{P}'_m(\xi_{m,z})}{\partial \mathbf{C}_{m,i}}, \tag{74}$$

and $\frac{\partial \mathscr{P}'_m(\xi_{m,z})}{\partial \mathbf{C}_{m,i}}$ follows directly from the derivative of B-spline basis functions.

A.4. Sensitivity of the fiber-content constraint

For the derivation of the local maximum fiber content constraint:

$$\frac{\partial g_{\mathrm{loc}}}{\partial \lambda} = \frac{1}{f_0}\frac{\partial \widetilde{f}_{\max}}{\partial \lambda} = \frac{1}{f_0}\frac{\partial \widetilde{f}_{\max}}{\partial \widetilde{f}_e}\frac{\partial \widetilde{f}_e}{\partial \lambda}, \tag{75}$$

where $\frac{\partial \widetilde{f}_{\max}}{\partial \widetilde{f}_e}$ is the standard p-norm weight. $\frac{\partial \widetilde{f}_e}{\partial \lambda}$ can be derived from Eq. (41).

$$\frac{\partial \widetilde{f}_e}{\partial \lambda} = \frac{\partial \rho_e}{\partial \lambda} f_e + \rho_e \frac{\partial f_e}{\partial \lambda}. \tag{76}$$

For the global fiber-usage constraint:

$$\frac{\partial g_{\mathrm{glob}}}{\partial \lambda} = \frac{1}{V_f N V_0}\sum_{e=1}^{N}\frac{\partial \widetilde{f}_e}{\partial \lambda}. \tag{77}$$

So far, the gradients of the objective and all constraints with respect to the design variables have been derived.

Data availability

No data was used for the research described in the article.

References

[1] J. Wong, A. Altassan, D.W. Rosen, Additive manufacturing of fiber-reinforced polymer composites: A technical review and status of design methodologies, Composites Part B: Engineering 255 (2023) 110603.
[2] R. Velu, Mechanical and self-monitoring properties of coextrusion 3D printed continuous carbon fibre reinforced polymer composites, Procedia CIRP 131 (2025) 74–79.
[3] P. Cheng, et al., 3D printed continuous fiber reinforced composite lightweight structures: A review and outlook, Composites Part B: Engineering 250 (2023) 110450.
[4] C. Tóth, B. Ilinyi, L. Kovács, Layer-level constitutive material model for representing non-linear stress-strain relationships in continuous carbon fiber-reinforced 3D-printed composites, Polymer Testing 146 (2025) 108794.
[5] Guo, P., et al., On the mitigation of the fiber breakage in material extrusion based additive manufacturing of carbon fiber reinforced polymer composites. Additive Manufacturing, 2025: p. 104896.
[6] Liu, C., et al., Novel 3D printed continuous fiber-reinforced composites: A strategy to realize spiral mode manipulating and support-free manufacturing. Additive Manufacturing, 2025: p. 104975.
[7] Z. Guo, et al., 3D printing of curvilinear fiber reinforced variable stiffness composite structures: A review, Composites Part B: Engineering 291 (2025) 112039.
[8] H. Zhang, et al., Multi-material 3D printing of continuous carbon fibre reinforced thermoset composites with tailored fibre paths and bespoke conforming thermoplastic moulds, Composites Part B: Engineering 298 (2025) 112373.
[9] W. Ye, et al., Additive manufacture of programmable multi-matrix continuous carbon fiber reinforced gradient composites, Additive Manufacturing 89 (2024) 104255.
[10] S. Wang, et al., A modified equally-spaced method (MEQS) for fibre placement in additive manufacturing of topology-optimised continuous carbon fibre-reinforced polymer composite structures, Composite Structures 335 (2024) 117998.
[11] M.P. Bendsøe, O. Sigmund, Material interpolation schemes in topology optimization, Archive of applied mechanics 69 (9) (1999) 635–654.
[12] M.Y. Wang, X. Wang, D. Guo, A level set method for structural topology optimization, Computer methods in applied mechanics and engineering 192 (1-2) (2003) 227–246.
[13] T. Yamada, et al., A topology optimization method based on the level set method incorporating a fictitious interface energy, Computer Methods in Applied Mechanics and Engineering 199 (45-48) (2010) 2876–2891.

[14] X. Huang, Y.M. Xie, Bi-directional evolutionary topology optimization of continuum structures with one or multiple materials, Computational Mechanics 43 (3) (2009) 393–401.
[15] X. Guo, W. Zhang, W. Zhong, Doing topology optimization explicitly and geometrically—a new moving morphable components based framework, Journal of Applied Mechanics 81 (8) (2014) 081009.
[16] W. Zhang, et al., A new three-dimensional topology optimization method based on moving morphable components (MMCs), Computational Mechanics 59 (4) (2017) 647–665.
[17] Zhou, L., W. Zhang, and V.B.C. Tan, Feature-driven concurrent optimization of composite topology and fiber orientation. International Journal of Mechanical Sciences, 2026: p. 111439.
[18] J. Liu, et al., Current and future trends in topology optimization for additive manufacturing, Structural and multidisciplinary optimization 57 (6) (2018) 2457–2483.
[19] Y. Guo, et al., Concurrent structural topology and fabrication sequence optimization for multi-axis additive manufacturing, Computer Methods in Applied Mechanics and Engineering 435 (2025) 117627.
[20] Y. Guo, et al., DGTO: Derivable geodesics-coupled topology optimization for multi-axis hybrid additive and subtractive manufacturing with curved layer generation, Additive Manufacturing 105 (2025) 104786.
[21] S. Xu, et al., Self-support structure topology optimization for multi-axis additive manufacturing incorporated with curved layer slicing, Computer Methods in Applied Mechanics and Engineering 438 (2025) 117841.
[22] S. Xu, et al., Topology optimization for hybrid additive-subtractive manufacturing incorporating dynamic process planning, Computer Methods in Applied Mechanics and Engineering 431 (2024) 117270.
[23] Y. Guo, et al., Deep learning-based topology optimization for multi-axis machining, Applied Mathematical Modelling 138 (2025) 115738.
[24] P. Sun, et al., Topology optimization of fiber-reinforced composite structures considering fiber orientation and cross-sectional size, Advances in Engineering Software 212 (2026) 104073.
[25] Y. Dong, et al., Strength-based concurrent topology and fiber orientation optimization considering different failure modes, Computer Methods in Applied Mechanics and Engineering 443 (2025) 118086.
[26] K. Liang, et al., DGTO: Derivable geodesics-coupled topology optimization for multi-axis 3D printing of continuous fiber-reinforced spatial structures, Computer Methods in Applied Mechanics and Engineering 448 (2026) 118419.
[27] Guo, Y., et al., Derivable geodesic weaving driven topology optimization for continuous and controlled-spacing fiber paths incorporating tension-compression anisotropy. Composites Part B: Engineering, 2026: p. 113604.
[28] Y. Dong, et al., Concurrent topology and fiber distribution optimization of continuous fiber-reinforced polymer (CFRP) structures under thermal-mechanical coupling, Acta Mechanica Sinica 42 (5) (2026) 424586.
[29] Y. Guo, R. Ahmad, Y. Ma, Topology optimization of the vibrating structure for fused deposition modelling of parts considering a hybrid deposition path pattern, International Journal of Computer Integrated Manufacturing 36 (9) (2023) 1379–1396.
[30] Nozawa, S. and G. Serhat, Topology and fiber path optimization of composite structures: A critical review. Materials & Design, 2025: p. 113699.
[31] Zhang, X., et al., A review of structural topology optimization for fiber-reinforced composites. Composites Part B: Engineering, 2025: p. 112393.
[32] B. Szederkenyi, N.K. Kovacs, T. Czigany, A comprehensive review of fiber-reinforced topology optimization for advanced polymer composites produced by automated manufacturing, Advanced Industrial and Engineering Polymer Research 8 (1) (2025) 113–131.
[33] Z. Yang, et al., Topology optimization of three-dimensional shell structures made of continuous fiber reinforced composites considering manufacturing constraints, Composites Part A: Applied Science and Manufacturing 198 (2025) 109069.
[34] Hou, Y., et al., Curvature-driven topology optimization of CCFRP composites. International Journal of Mechanical Sciences, 2026: p. 111202.
[35] K. Meng, et al., Dynamic topology optimization incorporating the material anisotropy feature for 3D printed fiber composite structures, Finite Elements in Analysis and Design 243 (2025) 104281.
[36] C. Wu, et al., Discrete topology optimization of ply orientation for a carbon fiber reinforced plastic (CFRP) laminate vehicle door, Materials & Design 128 (2017) 9–19.
[37] H. Ding, B. Xu, A novel discrete–continuous material orientation optimization model for stiffness-based concurrent design of fiber composite, Composite Structures 273 (2021) 114288.
[38] X. Xie, J. Bai, W. Zuo, Topology optimization of fiber-reinforced concrete structures using membrane-embedded model, Engineering Structures 314 (2024) 118299.
[39] W. Zuo, et al., Geometrically nonlinear topology and fiber orientation optimization of composite structures using membrane-embedded model, Thin-Walled Structures 203 (2024) 112250.
[40] T. Liu, et al., Neural co-optimization of structural topology, manufacturable layers, and path orientations for fiber-reinforced composites, ACM Transactions on Graphics (TOG) 44 (4) (2025) 1–17.
[41] A. Chandrasekhar, et al., FRC-TOuNN: Topology optimization of continuous fiber reinforced composites using neural network, Computer-Aided Design 156 (2023) 103449.
[42] D.R. Jantos, K. Hackl, P. Junker, Topology optimization with anisotropic materials, including a filter to smooth fiber pathways, Structural and Multidisciplinary Optimization 61 (5) (2020) 2135–2154.
[43] M.-P. Schmidt, et al., Structural topology optimization with smoothly varying fiber orientations, Structural and Multidisciplinary Optimization 62 (6) (2020) 3105–3126.
[44] D. Jiang, R. Hoglund, D.E. Smith, Continuous fiber angle topology optimization for polymer composite deposition additive manufacturing applications, Fibers 7 (2) (2019) 14.
[45] J. Wong, E.D. Sanders, D.W. Rosen, Topology optimization of additively manufactured continuous fiber-reinforced structures with constraints on fiber path geometry, Structural and Multidisciplinary Optimization 68 (5) (2025) 87.
[46] G. Ma, W. Yang, L. Wang, Strength-constrained simultaneous optimization of topology and fiber orientation of fiber-reinforced composite structures for additive manufacturing, Advances in Structural Engineering 25 (7) (2022) 1636–1651.
[47] X. Yan, et al., Concurrent topology optimization of structures and orientation of anisotropic materials, Engineering Optimization 52 (9) (2020) 1598–1611.
[48] Zhi, X., et al., Topology design of additively manufactured CFRP for impact resistance via B-spline-based Equivalent Static Load method. Composites Part B: Engineering, 2025: p. 112577.
[49] Y. Mori, R. Matsuzaki, N. Kumekawa, Variable thickness design for composite materials using curvilinear fiber paths, Composite Structures 263 (2021) 113723.
[50] Z. Yang, et al., Topology optimization of 3D-printed continuous fiber-reinforced composites considering manufacturability, Composites Science and Technology 230 (2022) 109727.
[51] X. Chen, et al., Field-based toolpath generation for 3D printing continuous fibre reinforced thermoplastic composites, Additive Manufacturing 49 (2022) 102470.
[52] T. Wang, et al., Load-dependent path planning method for 3D printing of continuous fiber reinforced plastics, Composites Part A: Applied Science and Manufacturing 140 (2021) 106181.
[53] V.S. Papapetrou, C. Patel, A.Y. Tamijani, Stiffness-based optimization framework for the topology and fiber paths of continuous fiber composites, Composites Part B: Engineering 183 (2020) 107681.
[54] T. Liu, et al., Stress-driven infill mapping for 3D-printed continuous fiber composite with tunable infill density and morphology, Additive Manufacturing 62 (2023) 103374.
[55] G. Li, Y. Chen, Q. Li, Strength-based collaborative topology optimization for continuous fiber reinforced composites, Computer Methods in Applied Mechanics and Engineering 430 (2024) 117206.

[56] G. Li, Y. Chen, Highly efficient and extensible parallel topology optimization for continuous fiber reinforced composites, Computer Methods in Applied Mechanics and Engineering 436 (2025) 117713.
[57] G. Li, X. Wang, Y. Chen, Three-dimensional topology optimization for continuous fiber reinforced composite thin-walled structures, Engineering with Computers 42 (1) (2026) 12.
[58] Y. Xu, et al., Topology optimization for additive manufacturing of CFRP structures, International Journal of Mechanical Sciences 269 (2024) 108967.
[59] T. Ho-Nguyen-Tan, et al., Anisotropic topology optimization and 3D printing for composite structures with tailored continuous carbon fiber paths, Composites Part B: Engineering 299 (2025) 112371.
[60] S. Xu, et al., A full-scale topology optimization method for surface fiber reinforced additive manufacturing parts, Computer Methods in Applied Mechanics and Engineering 401 (2022) 115632.
[61] H. Li, et al., Full-scale topology optimization for fiber-reinforced structures with continuous fiber paths, Computer Methods in Applied Mechanics and Engineering 377 (2021) 113668.
[62] H. Ren, et al., Concurrent optimization of structural topology and toolpath for additive manufacturing of continuous fiber-reinforced polymer composites, Computer Methods in Applied Mechanics and Engineering 430 (2024) 117227.
[63] H. Ren, et al., Manufacturability-aware topology and toolpath co-design for continuous fiber-reinforced composites additive manufacturing, Computer Methods in Applied Mechanics and Engineering 444 (2025) 118162.
[64] Z. Li, H. Xu, S. Zhang, A Comprehensive Review of Explicit Topology Optimization Based on Moving Morphable Components (MMC) Method, Archives of Computational Methods in Engineering 31 (5) (2024) 2507–2536.
[65] W. Hou, et al., Explicit isogeometric topology optimization using moving morphable components, Computer Methods in Applied Mechanics and Engineering 326 (2017) 694–712.
[66] B. Zhu, et al., Explicit structural topology optimization using moving wide Bezier components with constrained ends, Structural and Multidisciplinary Optimization 64 (1) (2021) 53–70.
[67] T. Shannon, et al., Generalized Bezier components and successive component refinement using moving morphable components, Structural and Multidisciplinary Optimization 65 (7) (2022) 193.
[68] Y. Zhou, et al., Worm-like highly deformable Multi-Section B-Spline Offset Feature for topology optimization, Computer Methods in Applied Mechanics and Engineering 412 (2023) 116108.
[69] Y. Zhou, et al., A bio-inspired B-spline offset feature for structural topology optimization, Computer Methods in Applied Mechanics and Engineering 386 (2021) 114081.
[70] R. Zheng, C. Kim, An enhanced topology optimization approach based on the combined MMC and NURBS-curve boundaries, International Journal of Precision Engineering and Manufacturing 21 (8) (2020) 1529–1538.
[71] Z. Sun, et al., Structural optimization of fiber-reinforced material based on moving morphable components (MMCs), Acta Mechanica Solida Sinica 35 (4) (2022) 632–646.
[72] G. Ren, et al., Multiscale topology optimization for fiber-reinforced composites based on moving morphable component (MMC) method, Structural and Multidisciplinary Optimization 68 (4) (2025) 80.
[73] A. Malakhov, A. Polilov, Design of composite structures reinforced curvilinear fibres using FEM, Composites Part A: Applied Science and Manufacturing 87 (2016) 23–28.
[74] K. Svanberg, The method of moving asymptotes—a new method for structural optimization, International journal for numerical methods in engineering 24 (2) (1987) 359–373.
[75] J. Zhao, CFRCTop: An Efficient MATLAB Implementation for Topology Optimization of Continuous Fiber-Reinforced Composite Structures, Applied Sciences 15 (17) (2025) 9242.
[76] X. Yan, et al., Manufacturing-oriented topological design of CFRC structures with variable fiber volume and orientation, Composite Structures 310 (2023) 116779.
[77] J. Zhao, T. Qi, C. Wang, Efficient GPU accelerated topology optimization of composite structures with spatially varying fiber orientations, Computer Methods in Applied Mechanics and Engineering 421 (2024) 116809.
[78] T. Qi, J. Zhao, C. Wang, An efficient GPU solver for 3D topology optimization of continuous fiber-reinforced composite structures, Computer Methods in Applied Mechanics and Engineering 435 (2025) 117675.